Journal of Electroceramics (2018) 40:271–292
https://doi.org/10.1007/s10832-018-0128-z

FEATURE ARTICLE

Accelerated microwave-assisted hydrothermal/solvothermal processing: Fundamentals, morphologies, and applications

Cecilia A. Zito[1] · Marcelo O. Orlandi[2] · Diogo P. Volanti[1]

Received: 31 May 2016 / Accepted: 28 February 2018 / Published online: 12 March 2018

Abstract
This article is designed to serve as a roadmap for understanding the fundamentals, the key advantages and the potential applications of microwave-assisted hydrothermal/solvothermal (MAH/S) processing. MAH/S synthesis is a versatile chemical method for preparing a diversity of materials such as metals, semiconductors, electroceramics, graphene and their composites as bulk powders, thin films, or single crystals. The key to improve performance of these materials is achieving controlled morphologies (0 to 3D dimensionality) that favor desirable physical-chemical phenomena at the surface, and in the bulk of these advanced materials. The main features related to the improvement of the thermal and non-thermal effects associated with the use of microwave power concurrently with hydrothermal or solvothermal methods are discussed. Furthermore, the main crystal growth mechanisms (Ostwald ripening and oriented attachment) of these solids in solution under MAH/S treatment are described. Products synthesized by the MAH/S, particularly of interest in the development of gas sensors, batteries, fuel cells, solar cells and photocatalysts are emphasized. We conclude by envisaging new future directions for the use of this rapid and versatile processing approach.

Keywords Composites · Microwave · Graphene · Metal oxides · Nanostructures · Crystal growth

1 Introduction

Microwave-assisted hydrothermal/solvothermal (MAH/S) synthesis is a chemical method for preparing a diversity of materials such as metals [1–3], semiconductors [4–6], electroceramics [7–10], graphene composites [11–15], as well as many other types of materials. The process involves the use of water (hydrothermal), different solvents (solvothermal) or mixtures of both, as synthetic medium under pressure, typically above the solvent vapor pressure and temperature near or above its boiling point in a sealed pressurized vessel during microwave (MW) irradiation (typically 2.45 GHz frequency). The method is quite versatile and can be used in preparation of bulk powders [7, 9, 16], thin films [17, 18], single crystals [19–21], polycrystalline compounds [22–25], and composites [11, 13, 26, 27]. In addition, it is possible to obtain different crystal morphologies — three-dimensional (3D) [28–32], two-dimensional (2D) [33–35], one-dimensional (1D) [36–38], or zero-dimensional (0D) [2, 39–43], by controlling the solvent supersaturation, precursor concentration, use of templates, pH adjustment, kinetic control, and other parameters. Furthermore, this procedure represents an interesting alternative to others for the preparation of new thermodynamically stable or even metastable materials. Over the last decade, a large number of reports regarding MAH/S synthesis have focused on controlled materials morphology (Fig. 1). This review highlights the advances in fundamental aspects of MAH/S synthesis, and provides examples and applications of materials prepared by this method.

We present an overview of the experimental aspects and the basic principles concerning morphology and size control, thermodynamic and kinetic factors, classical and non-classical crystal growth mechanisms during MW heating. This is followed by describing the main features that induce the choice of this technique and correlate it with the versatility of obtaining large numbers of advanced materials of different compositions ranging from metallic nanoparticles, n- and p-

✉ Marcelo O. Orlandi
orlandi@iq.unesp.br

[1] Laboratory of Materials for Sustainability, IBILCE, São Paulo State Univeristy – UNESP, São José do Rio Preto 15054-000, Brazil

[2] Interdisciplinary Laboratory of Ceramics, IQ, São Paulo State University – UNESP, Araraquara 14800-060, Brazil

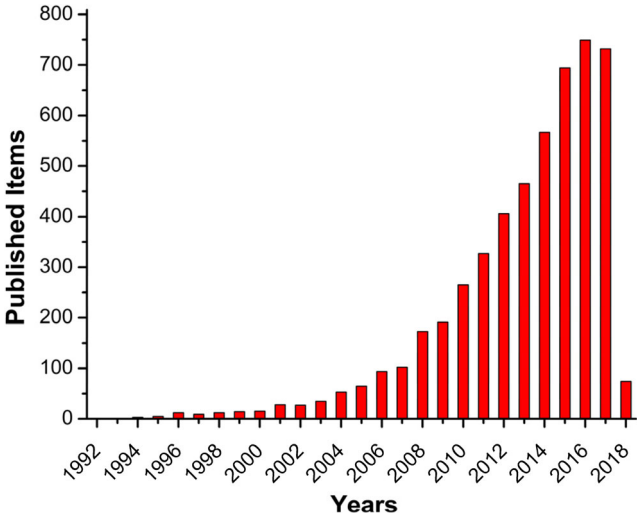

Fig. 1 The number of published items in each year on microwave-assisted hydrothermal/solvothermal processing. Data collected from the "Web of Science" in February 2, 2018. The words "microwave and (hydrothermal or solvothermal)" were input into the "topic" search box.

type semiconducting metal oxides, electroceramics, graphene and diverse composite materials. In addition, it will be shown that these MW-assisted synthesized materials have potential application in certain technological areas of high interest such as gas sensors, photocatalysts, fuel cells, batteries and solar cells. Figure 2 shows a schematic representation of the possibilities arising from the methods discussed here. Finally, through an examination of the trends described in the literature, new future research directions for materials synthesis by the MAH/S method will be described.

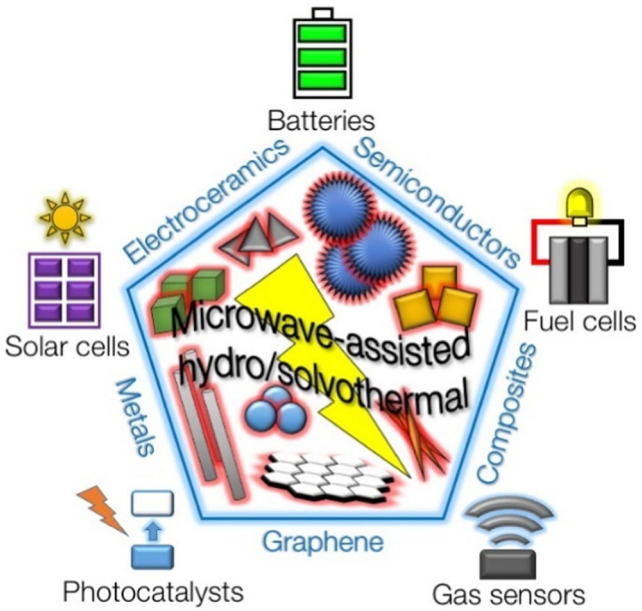

Fig. 2 An overview of the possible applications of the MAH/S method for obtaining materials with different compositions and morphologies of relevance to advanced technological applications

2 Effects of microwave power on hydrothermal/solvothermal synthesis

In general, the conventional hydrothermal/solvothermal methods refer to the processes taking place in closed systems where reagents and solvents are treated under both medium to high pressure and medium to high temperature. The most recognized delineation of the "hydrothermal" method relates to a heterogeneous reaction medium containing water as a main solvent (usually at a temperature above 100 °C and at a pressure above 1 atm) [44–47]. Modified conditions are typically achieved either by using an autoclave, a vessel allowing the exposure of selected materials to relatively elevated pressure and temperature by subjecting them to high-pressure saturated steam, or by employing a specific reactor to generate autogenous pressure through the heating of the closed reactor [48].

On the other hand, the addition of microwave power under hydrothermal/solvothermal conditions can contribute to remarkable improvements in the organic materials synthesis process/organic materials synthesis process. This is related to increased reaction rates induced by high temperatures; improved control of reaction parameters; improved reproducibility; superior yields; improved synthesis product selectivity resulting from reduced side reactions; indirect interaction between the microwaving source (magnetron valve) and the solvents and/or reactants; selective heating (if there are products with different microwave susceptibility in the reaction mixture); automatization and high throughput synthesis [49]. Varma and co-authors [50–57] described several microwave approaches leading to *greener* methods for producing nanocatalysts; use of recyclable mineral oxides or supported reagents; synthesis of pharmaceutically active heterocycles; organics and nanomaterials. Such advantages arise from the physical mechanisms inherent to the dielectric fluid heating phenomenon via microwave susceptibility described below.

Conventional heating of a solution occurs by heat conduction along the walls of the reaction vessel followed by diffusion to the central volume of the solution. In this less efficient process, there is loss of heat energy as well as non-uniform heating of the reaction medium. This leads to unequal distribution with some regions more heated than others, which results the need of extra time to obtain the final product. In the case of solid growth, this favors crystallization with a broad size distribution.

To circumvent these problems, using microwave as the heat source is a more efficient alternative. Microwaves induce dielectric medium heating and do not rely on heat conduction. The two most widely accepted mechanisms for explaining the instantaneous heating caused by microwaves are dipole rotation and ionic conduction [58–60]. In the first mechanism, polar molecules of certain solvents interact with the electric field component of the microwave through dipole rotation,

with these movements leading to heating of the entire solution. In the second case, the ionic species present in solution respond quickly to the microwave driven force, causing rapid heating due to Joule heating. As the temperature increases, the energy transfer is more efficient and the whole process is facilitated.

Microwaves contribute to high yield given the rapid consumption of the initial reagents promoted by increased reaction kinetics and initial rapid heating [61]. In contrast to conventional heating where heat is dissipated at the walls of the reactor vessel, heating by microwaves takes place uniformly within the entire volume susceptible to the radiation (Fig. 3). Thus, microwave-based system may reach the boiling temperature of the solvent by 10 to 1000 times faster than the conventional system [62].

It is noteworthy that the microwaves do not have sufficient energy to break chemical bonds, but it is speculated that non-thermal microwave effects can increase the effective collisions between the molecules of the reagents and solvents [63–65]. Moreover, the conformation of the microwave apparatus can also influence the final results and the reproducibility of the experiments [66]. The Arrhenius equation [$k = A\ \exp.(-Ea/RT)$], where k is the rate, A is the molecular collisions pre-exponential constant, Ea is the activation energy and R is the gas constant; can be used to indicate the relationship between $k \propto A$ at constant temperature (T) under MW heating. Typical chemical reactions result from specific molecular collisions, which classically increase with increasing temperature but also result from MW non-thermal effects. Nevertheless, for an specific reaction it is difficult to differentiate the specific molecular collisions effect from the impact of the temperature average molecular motion [67].

Accordingly, the choice of a suitable solvent (with appropriate permanent dipole moment) is vital to achieve the desired selective heating for the growth of homogeneously crystallized particles while achieving improved size distribution in reduced time. Importantly, microwave heating can accelerate slow reactions with associated large activation energies.

To illustrate the synergistic use of microwave power with the hydrothermal/solvothermal methods, Table 1 lists materials for which the addition of microwave power was observed to accelerate synthesis compared to the conventional hydrothermal/solvothermal process. Reaction times can be reduced from hours for conventional methods to minutes for microwave synthesis of the same crystalline structure materials.

3 Morphology control and growth mechanisms during MW irradiation

To improve the performance of functional materials, it is very important to have fine control over the shape and size of particles. In many cases the form of a crystalline solid derives from its unit cell structure. Wulff's thermodynamic study [81] indicates that solids may have different morphologies because of the different surface energies of the crystal face during growth in a given environment. The lowest free energy will be associated with the more stable faces during the growth process, culminating in the formation of crystals with morphology having lowest surface energy [82].

Considering that the Wulff criteria also relates to growth within microwave-assisted hydrothermal/solvothermal reactions, Andrés et al. [83] developed a combined theoretical

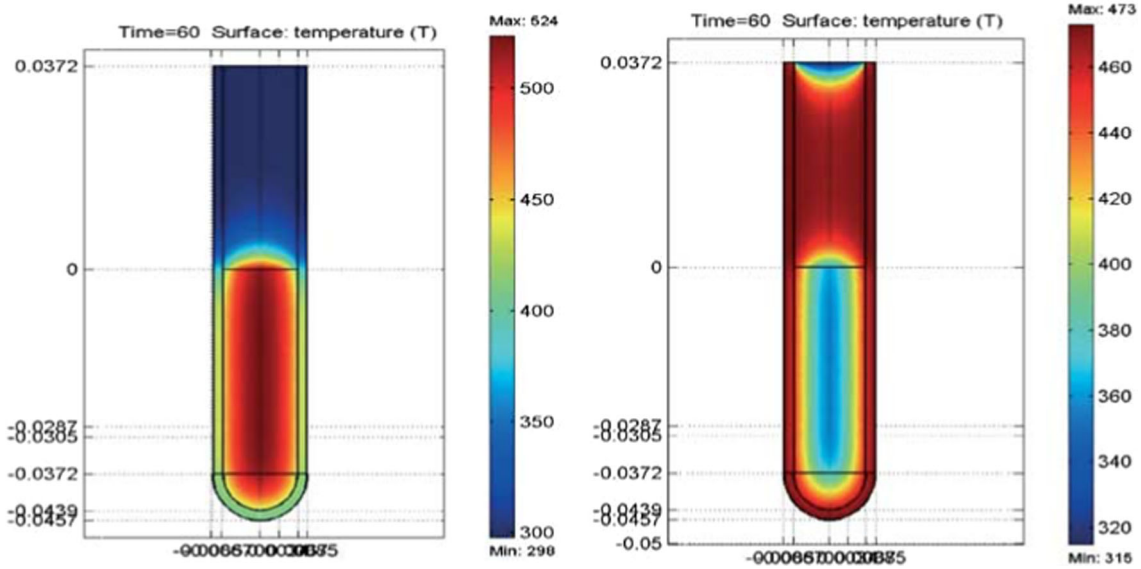

Fig. 3 (Left). The microwave effect on the temperature profile after 60 s exposure. (Right). Comparison with a temperature profile of an oil bath. Heating by microwaves is more homogeneous in the central volume of the solution. The temperature range is in Kelvin and the position of the meniscus is indicated at the zero vertical axis. Reproduced with permission from Ref. [62], Copyright (2003) Springer

Table 1 Examples of microwave effect on hydrothermal/solvothermal synthesis. The same material can be obtained in shorter time or lower temperature in given solvents

Material formula, crystalline phase	Method of synthesis	Solvent	Reaction time, temperature	Ref.
CuO, monoclinic	Hydrothermal	Water	10 h, 100 °C	[68]
CuO, monoclinic	Microwave-assisted hydrothermal	Water	15 min, 100 °C	[69]
SnO_2, tetragonal	Solvothermal	Ethanol	24 h, 285 °C	[70]
SnO_2, tetragonal	Microwave-assisted solvothermal	Water/ethanol	15, 20, 30, 45, 60, and 90 min; 240 °C	[71]
Fe_3O_4, face centered cubic	Solvothermal	Ethylene glycol	12 h, 200 °C	[72]
Fe_3O_4, face centered cubic	Microwave-assisted hydrothermal	Water	2 h, 150 °C	[43]
SnO_2-RGO, tetragonal for SnO_2	Hydrothermal	Water	12 h, 180 °C	[73]
SnO_2-RGO, tetragonal for SnO_2	Microwave-assisted sol-gel method	Benzyl alcohol	10 min, 185 °C	[74]
Cu@Cu_2O, cubic	Solvothermal	Toluene and water	12, 24 and 48 h, 200 °C	[75]
Cu/Cu_2O, cubic	Microwave-assisted hydrothermal	Water	5, 10, 20, 30 and 60 min, 100 °C	[76]
ZnO, hexagonal	Solvothermal	Methanol or Ethanol	24 h, 120 °C	[77]
ZnO, hexagonal	Microwave-assisted solvothermal	Ethanol or ethylene glycol	5 min, 180 °C	[78]
TiO_2, tetragonal anatase	Solvothermal	Isopropanol	72 h, 170 °C	[79]
TiO_2, tetragonal anatase	Microwave-assisted hydrothermal	Water	1 h, 180 °C	[80]

(first-principles calculations) and experimental study to improve the understanding of the electronic energy and structural properties that induce the control of the morphology of different metals and metal oxides, such as TiO_2, $BaZrO_3$, α-Ag_2WO_4 and Ag. Figure 4 shows the good agreement between the scanning electron microscopy (SEM) image of $BaZrO_3$ crystals obtained by microwave-assisted hydrothermal (MAH) and the theoretical surfaces predicted by the Wulff simulation.

The classic process of solid crystallization in supersaturated solution follows a bottom-up design, starting from atoms, molecules or clusters using thermodynamics as the driving force. In order to prepare supersaturated solutions, changes in temperature or pressure, additions of soluble salts and/or changes of pH in solution are necessary [84, 85]. Under the MW-assisted hydrothermal/solvothermal method, different types of nucleation and growth processes are observed which are earlier than the conventional heating technique. In this section, the two main nucleation and growth mechanisms (Ostwald ripening and oriented attachment) that govern crystallization of inorganic solids will be described and illustrated. The growth of materials in the hydrothermal/solvothermal medium is impacted by both thermodynamic and kinetic parameters. Figure 5 illustrates the steps for mineral crystallization which arises from changes in the activation energy barriers related to nucleation, crystal growth and possibly phase changes [86].

The Ostwald ripening (OR) mechanism [87] occurs due to the change in solubility of the nanoparticles in solution. Smaller particles have larger surface energy and a higher solubility facilitating their redissolution and subsequent aggregation onto existing larger particles. For this type of growth to take place, it is essential that the chemical potential of the nanoparticles increases in the process of dissolution and new precipitation, culminating into the growth of particles at the expense of the decrease in the total number of particles present

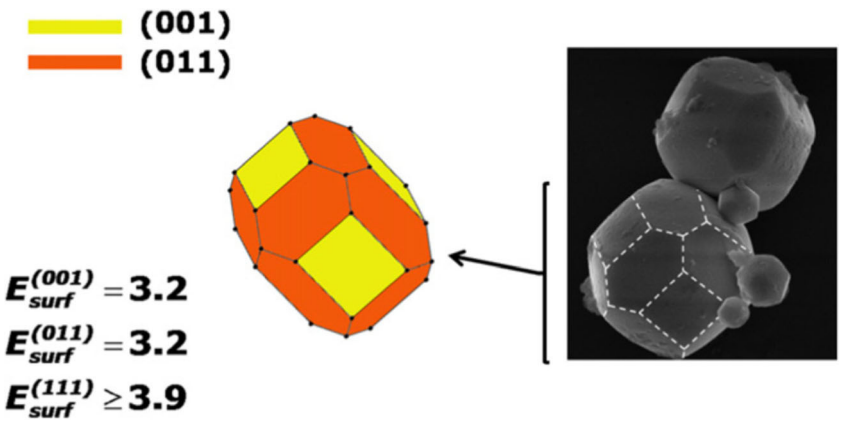

Fig. 4 (Left). The Wulff crystal representation of $BaZrO_3$ material with surface energy in Joules per square meter. (Right). Scanning electron microscopy image of $BaZrO_3$ crystals obtained by microwave-assisted hydrothermal method. Reproduced with permission from Ref. [83], Copyright (2015) IOP Publishing

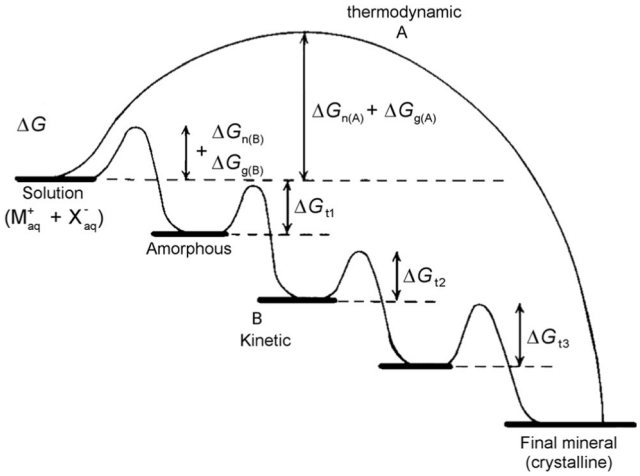

Fig. 5 The influence of the kinetics and thermodynamics in the crystallization process. Mineral crystallization can occur in a single stage (A) or through a sequence of steps (B) depending on the free energy of activation in accordance with the processes of nucleation, growth and phase transformation with amorphous phases representing possible kinetic reaction intermediates. Reproduced with permission from Ref. [86], Copyright (2003) Wiley-VCH

in solution until the equilibrium state is reached. According to the Thomson-Gibbs equation, the fluidity of the smaller particles to the larger surface occurs due to the shift of the local chemical potential of the solution. This process is usually controlled by diffusion; and the final result is the production of near-spherical particles which are more thermodynamically stable [88]. Thus, the events described above take place during the growth of the particles in the MAH/S method. However, the nucleation process is faster and more homogeneous with the aid of microwave heating, promoting more effective maturation of the desired crystals. There are many published studies indicating that OR mechanism is responsible for the production of different types of materials [76, 89–92].

The oriented attachment (OA) mechanism was first described by Penn et al. [93] to explain how titania nanoparticles aggregate during hydrothermal synthesis leading to their growth into the final crystalline form. In the OA process, there is a spontaneous local organization (in planar interface) of close particles having similar crystallographic orientation [94], which requires the continued alignment of common crystal planes during crystal growth [95]. This type of non-classical mechanism helps to explain the formation of nanocrystals with controlled morphology by the assembly of primitive oriented crystallites available in solution. However, it is necessary to use modern techniques of characterization to identify and to explain in detail the mechanism in solution [96]. The use of microwave radiation provides a rapid and homogeneous heating of solution, in addition to possibly assisting in the alignment of the atomic planes by dipole rotation. Recent literature shows that materials grown by MAH/S occur via OA [40, 69, 97, 98]. Some reaction conditions, morphology and nucleation/growth mechanisms for metal oxides/hydroxides are summarized in Table 2.

4 Examples of microwave-assisted hydrothermal/solvothermal materials synthesis

The first paper which describes the MAH/S synthesis was reported in 1992 by the Komarneni group, in which crystalline oxides, such as TiO_2, ZrO_2, Fe_2O_3, $KNbO_3$ and $BaTiO_3$, were prepared using a combination of 2.45 GHz microwaves and hydrothermal techniques [102]. In recent years, many papers describing the use of microwave-assisted methods have been published, and these include Bilecka and Niederberger, who demonstrated the liquid phase routes for synthesizing inorganic nanomaterials [49], and the Kappe group, that elucidated the role of microwave irradiation in the synthesis of colloidal inorganic nanocrystals [103], drug discovery [104], and organic synthesis [105, 106]. In the following sections, we present examples of metallic nanoparticles, metal oxide semiconductors, electroceramics, and composites synthesized by MAH/S method. In addition, we described the morphologies, reaction time, temperature, solvents, precursors, and the surfactant agents.

4.1 Metallic nanoparticles

4.1.1 Ag, Au, Pt and Pd

A rapid microwave-polyol method for preparation of silver (Ag) and platinum (Pt) nanoparticles (NPs) was described by Komarneni and co-authors [107]. They produced NPs in 15 min, much faster than the conventional polyol method. They also showed that the size of Pt nanoparticles depends on the molecular weight of the polyvinylpyrrolidone (PVP) polymer. Nadagouda and Varma [53] also reported the synthesis of Ag nanoparticles without the use of surfactants or reducing agents, showing that the NPs were only obtained in higher polyethylene glycol concentration. In Gao's work [1], Ag nanoparticles were prepared under microwave-assisted solvothermal conditions, in which different ratios of ethylene glycol and dodecylthiol were used to modify the particle morphology, a result of changes in reducing rate caused by the interaction between dodecylthiol and silver ions. Ag, Au, Pd and Pt nanoparticles were successfully prepared under microwave irradiation using glutathione as reducing and capping agent in aqueous medium. For Ag nanoparticles, the size ranged from 5 to 10 nm, while for the other metals larger particles were obtained (100–120 nm) [57]. Palladium NPs with about 3.8 nm of diameter were successfully prepared by MA solvothermal

Table 2 Synthesis of metal oxides/hydroxides by MAH/S method, highlighting the main experimental conditions, crystallographic/morphological characteristics, and nucleation/growth mechanisms

Material formula, crystalline phase	Precursor	Solvent	Solvent additives	Nucleation/ growth mechanisms[a]	Morphology	Ref.
ZnO, hexagonal	$Zn(O_2CCH_3)_2{\cdot}2\,H_2O$	N,N-dimethylformamide (DMF) and water	polyvinylpyrrolidone (PVP)	OA	Twinned-nanostructures	[97]
α-Fe_2O_3, hexagonal	$Fe(NO_3)_3{\cdot}9\,H_2O$	Water and ethanol	polyvinylpyrrolidone (PVP)	OA	Mesoporous microspheres	[98]
CeO_2, cubic	$Ce(NO_3)_3{\cdot}6H_2O$	Water	None	OR	Hollow nanospheres	[99]
CuO, monoclinic	$CuCl_2{\cdot}2H_2O$	Water	None	OR	Plates	[91]
SnO_2, tetragonal	$SnCl_4.5H_2O$	Water and Ethanol	NaOH	OR	Nanorods	[71]
β-$Ni(OH)_2$, hexagonal	$Ni(NO_3)_2.6H_2O$	Water	Cetyltrimethyl ammonium bromide (CTAB), ammonia	OA	Nanoflakes	[100]
Cu-Cu_2O, cubic	$[Cu(OAc)_2.H_2O]$	Water	Polyvinylpyrrolidone (PVP), ascorbic acid	OR	Thick/thin-shell hollow spheres	[76]
TiO_2, tetragonal anatase	Titanium tetraisopropoxide	Water	Tetramethylammonium hydroxide (TMAOH), citric acid	OA	Nanorods and V-shaped twins	[80]
$WO_3{\cdot}0.33H_2O$ orthorhombic	$Na_2WO_4{\cdot}2H_2O$	Water	None	OR	Nanocolumn bundle-like	[101]

[a] *OA* Oriented attachment, *OR* Ostwald ripening

method, using ethanol solution of $Pd(OAc)_2$ and PVP. In this case, 5 min of microwave exposition was sufficient to reduce Pd(II) to Pd(0) [3].

4.1.2 Metallic alloys

Au/Pd particles were synthesized starting from palladium powder and muriatic solution of gold by microwave and conventional hydrothermal methods. The microwave treatment was more efficient in achieving homogeneity of particles than conventional heating [108]. Nguyen et al. [109] reported the synthesis of FePt using platinum acetylacetonate and disodium tetracarbonylferrate as precursors with oleyl amine and octyl ether at 280 °C. They verified that the microwave heating at high pressure resulted in a mixture of face-centered cubic and face-centered tetragonal structured FePt particles. The alloy Au/Au_xPd_{1-x}, in which Au is the core and Au_xPd_{1-x} is the shell, was processed via layer-by-layer growth, resulting in a uniform morphology for all nanoparticles. The synthesis by the MAH method was performed in only 3 min using gold nanoparticles, gold and palladium salts, and sodium citrate as reducing agent [110]. A layer-by-layer formation of Au/Ag nanoparticles, with Au core and Ag shell, was also reported [111]. Figure 6 shows the images from transmission electron microscopy (TEM) of two nanoparticles prepared at 120 °C, where the number of shell layers is equal to 10. It shows the formation of the core-shell structure along with the dimensions of the shell thickness and core diameter.

4.2 N-type metal oxide semiconductors

Metal oxide semiconductors (MOS) have attracted a great deal of interest given their wide range of applications, as discussed in the final section of this review. Among the different n-type MOS, the most common are SnO_2, WO_3, In_2O_3, Fe_3O_4, ZnO and TiO_2, which will serve as the focus of our discussion. An overview of the morphologies obtained for these n-type materials can be seen in Fig. 7. It includes SnO_2 nanosheets [112], WO_3 spheres [113], ZnO flower-like [114] and In_2O_3 bundle-like structures [115].

4.2.1 SnO_2

Birkel et al. [71] closely monitored the crystal growth of SnO_2 nanorods prepared by a microwave-assisted reaction and recorded the process by a series of photographic images. In the early minutes of the reaction (15 min.), ill-defined rod-like structures were obtained mixed with other morphologies (spheres and cubes). These structures served to initiate the growth process resulting in nanorods final morphology after 45 min of reaction. Keeping the synthesis running for longer times (60–90 min.), rods size and crystallinity further increased.

Wang et al. [112] compared the performance of photoanodes of dye-sensitized solar cells that consists of SnO_2 nanosheets prepared by MAH and conventional hydrothermal synthesis. Both methods led to the same general nanosheet morphology, but the sheet size produced by

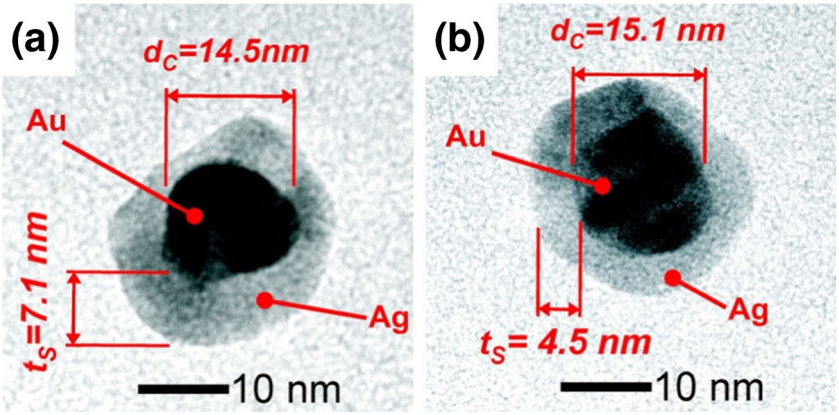

Fig. 6 (**a**, **b**) High resolution transmission electron microscopy (TEM) images of Au/Ag nanoparticles. d_c = core diameter, t_s = shell thickness. Adapted with permission from Ref. [111], Copyright (2011) American Chemical Society

MAH was smaller due to faster heating resulted in a high nucleation density within a short time. This led to enhanced photoelectrical energy conversion efficiency. Figure 7(a) presents nanosheets prepared by the MAH method.

The influence of ethanol/water ratio on the growth of SnO_2 nanoparticles was studied by Mansek and co-workers [116]. It was demonstrated that the higher the ethanol/water ratio, the bigger the nanoparticle size, but when only ethanol was applied as solvent no particles were formed, thus, revealing a mechanism of SnO_2 synthesis based on the hydrolysis process.

4.2.2 WO_3

Phuruangrat et al. [117] prepared the hexagonal phase of WO_3 by both MAH and conventional hydrothermal methods which led to nanowire and nanorod morphologies, respectively. The WO_3 nanowires produced by MAH within 3 h exhibited both higher crystallinity and aspect ratio (over 625) than the WO_3 nanorods prepared by CH method in 12 h, both at 150 °C. It was found that the WO_3 nanowires had superior electrocatalytic activity for the hydrogen evolution reaction from water, compared to WO_3 nanorods due to their high crystallinity and aspect ratio.

WO_3 hierarchical nanospheres were synthesized by MAH at 180 °C for 10, 30, 60 and 240 min, in order to evaluate the effect of synthesis time. The morphology of the nanospheres produced within 10 min is illustrated in the SEM image of Fig. 7(b). The diameter and dispersion of the spheres increased with time until 240 min, after which the homogeneity of the spheres disappeared [113]. Sungpanich et al. [118] also studied the influence of time on the synthesis of WO_3 nanoplates. For reaction times equal to or below 120 min, two different phases (monoclinic WO_3 and orthorhombic $WO_3.H_2O$) were obtained, while at reaction time of 180 min only monoclinic WO_3 nanoplates were obtained.

WO_3 hydrates have also been prepared by the MAH method. Perfecto et al. [119] demonstrated the synthesis of nanostructured $WO_3 \cdot 0.33H_2O$ by a synthetic approach combining ultrasonic spray nozzle and MAH methods. The crystal growth was discussed in two steps, as depicted in Fig. 8. First, the ultrasonic spray nozzle step enhances the nucleation rate of H_2WO_4 clusters. Then, during the MAH step, the particles grow in nanocolumn shape by Ostwald ripening process and are self-assembled into a hierarchical morphology. As a result of the developed synthetic method, the hierarchical $WO_3 \cdot 0.33H_2O$ nanocolumns showed a high specific surface (125 $m^2\ g^{-1}$) area and exhibited excellent isopropanol sensing performance at room temperature.

4.2.3 ZnO

Different morphologies of ZnO were effectively obtained using a MAH method by changing the solvents and precursors, as well as applying different reaction times, in the absence of templates or surfactants (Fig. 9). The growth processes for each reaction condition were discussed, showing the role of the solvents (water, ethanol and ethylene glycol) in achieving marigold flower-like, jasmine, sea urchin-rod, calendula, and rice grain shape-like morphologies [78].

The nanorod morphology is commonly observed for ZnO synthesized by MAH. Although the reaction time was shortened, surfactant cetyltrimethylammonium bromide was required as a structure directing agent in the synthesis [120]. Pimental et al. [114] studied the effect of time and microwave power on ZnO synthesis. They observed that increasing MW power, resulted into thinner nanorods, until flower-like structures appeared. For example, Fig. 7(c) shows a flower-like structure of ZnO that was obtained using 450 W for 6 min. In this study, the same morphology was achieved by conventional hydrothermal method, taking at least 4 h compared to 6 min for the MAH treatment. Flower-like ZnO morphology

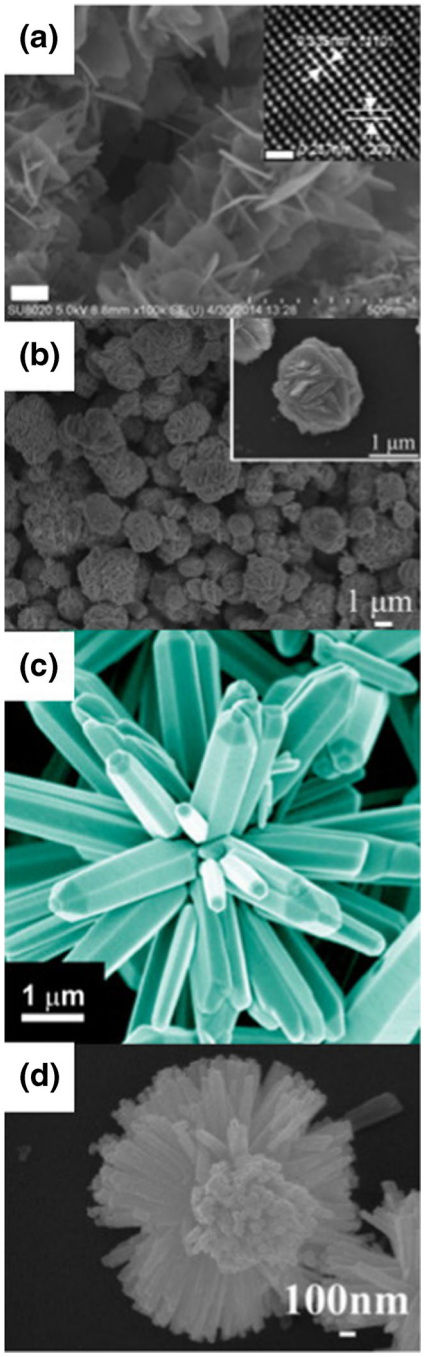

Fig. 7 SEM images of: (**a**) SnO_2 nanosheets (scale bar denotes 100 nm), inset: high resolution TEM (scale bar denotes 1 nm), showing the lattice spacing of SnO_2. Adapted with permission from Ref. [112], Copyright (2014) American Chemical Society; (**b**) WO_3 hierarchical spheres prepared in 10 min, inset: a single hierarchical sphere. Adapted with permission from Ref. [113], Copyright (2014) The Royal Society of Chemistry; (**c**) ZnO flower structure obtained using 450 W for 6 min. Adapted with permission from Ref. [114], Copyright (2014) American Chemical Society; (**d**) In_2O_3 bundle-like structure assembled out of 1D nanorods. Adapted with permission from Ref. [115], Copyright (2015) Elsevier. All materials were prepared by the MAH/S method

obtained by MAH method also exhibited excellent radiation sensing response at room temperature [121].

4.2.4 In_2O_3

Rapid synthesis of In_2O_3 using vitamin C as a structure-directing agent was reported by Li et al. [115]. They discussed the formation of cubic In_2O_3 with nanorod bundle-like morphology (Fig. 7(d)), achieved at 140 °C. The morphologies appeared to evolve following the increase in temperature; e.g., samples prepared at 115 and 120 °C were elliptical nanoparticles with smooth surfaces or with small protuberances on the surfaces, respectively; while the ones synthesized at 130 °C were composed of 1D nanorods. Finally, nanorod bundles were obtained at 140 °C. Motta and co-workers [122] described the synthesis of $In(OH)_3$ by the MAH method, followed by annealing at 500 °C for 5 min in a microwave oven. Cubic and rectangular shapes of $In(OH)_3$ and In_2O_3 were reported, with collapse of the structures due to water elimination following annealing.

4.2.5 Fe_3O_4

Magnetite (Fe_3O_4) has attracted attention for in Li-ion battery applications, for electronic devices and as support for catalyst immobilization, due to its magnetic properties. Rizzut et al. [43] found that the morphology of Fe_3O_4 was influenced by the different additives used in the synthesis. The use of PVP polymer promoted the formation of hexagonal nanoplates, similar to that found in synthesis without additives, whereas the use of trisodium citrate and oleic acid resulted in spheroidal and quasi-spherical nanoparticles, respectively.

Chen et al. [123] reported the synthesis of Fe_3O_4 by MAH using only $FeCl_2$ and NaOH. By increasing the reaction temperature to 50 °C trace amounts of Fe metal were observed, at the same time there was an improved development of the Fe_3O_4 faces. Fe_3O_4 nanoparticles were synthesized with low reaction time (30 min.) and changes in the precipitating and nucleating agents [90]. Pure Fe_3O_4 cubic phase could only be obtained using aqueous ammonia, while the use of $(NH_4)_2CO_3$, NH_4HCO_3 or NH_4Ac led to the formation of other phases (FeO(OH) and α-Fe_2O_3). Furthermore, polyhedral nanoparticles with uniform-shapes were obtained with aqueous ammonium and ammonium bicarbonate, whereas clusters appeared when ammonium carbonate or acetate was used.

4.2.6 TiO_2

Titanium dioxide (TiO_2) is central to a number of applications such as solar cells [80, 124, 125], batteries [126], and photocatalysis [127]. For the dye-sensitized solar cell application, a low-cost, clean and rapid synthesis of TiO_2 using MAH method has been proposed. Nanorods and V-shaped twin morphologies of TiO_2 were prepared by using mixtures of

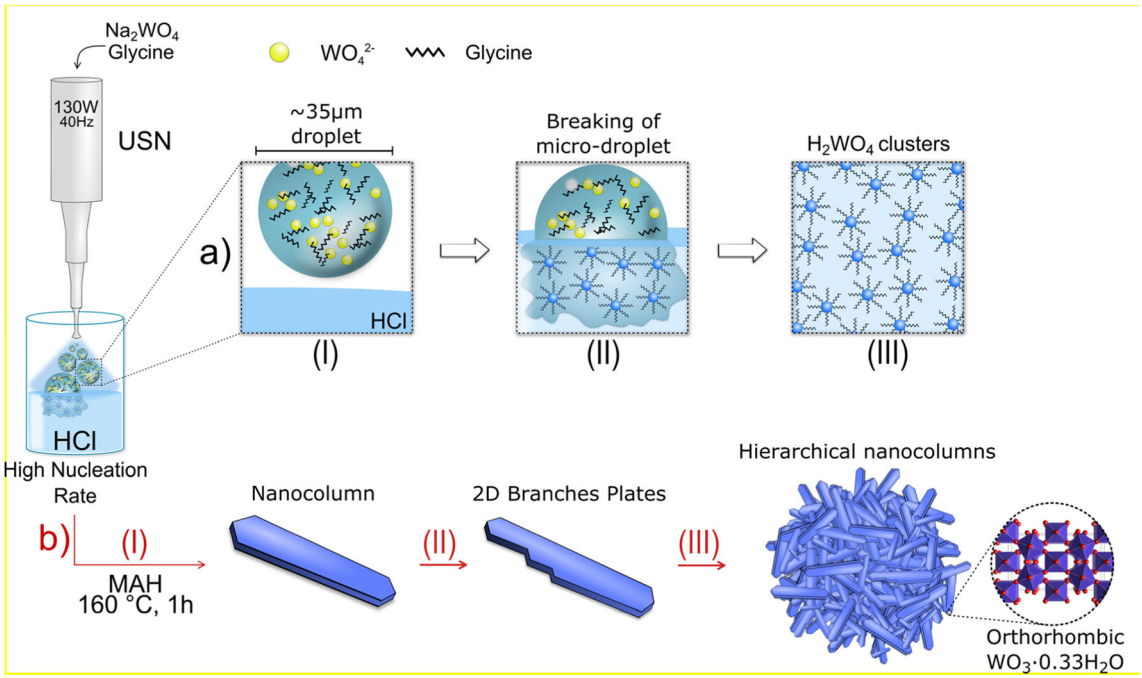

Fig. 8 Crystal growth illustration of nanostructured $WO_3 \cdot 0.33H_2O$ using a combination of ultrasonic spray nozzle and MAH methods. The growth mechanism can be divided in two steps: (**a**) high nucleation rate of H_2WO_4 clusters and (**b**) growth of nanocolumns by Ostwald ripening followed by the self-assembly of the structures until the final hierarchical morphology is achieved. Reproduced with permission from Ref. [119]. Copyright (2017) The Royal Society of Chemistry

titanium tetraisopropoxide, tetramethylammonium hydroxide (TMAOH), and citric acid in aqueous medium, heated at 180 °C for 60 min. This method resulted in particles of TiO_2 with a highly crystallized nature, exhibiting high incident photon-to-current conversion efficiency (85.6%) [80]. Shen et al. [125] reported a solvothermal route for the synthesis of TiO_2 nanocrystals, carried out by reacting titanium isopropoxide, isopropanol and water for 30 min at 220 °C.

Yoon and co-workers [126] demonstrated that different polymorphs of TiO_2 could be obtained by the use of diverse alcohols as solvents and changing the titanium source ($TiCl_3$ or $TiCl_4$) in the synthesis. For instance, when using ethanol and $TiCl_4$ or $TiCl_3$, the resulting phase was tetragonal anatase. On the other hand, the use of butanol with $TiCl_4$ led to the formation of tetragonal anatase, but with $TiCl_3$ orthorhombic brookite, with a small amount of tetragonal rutile, was

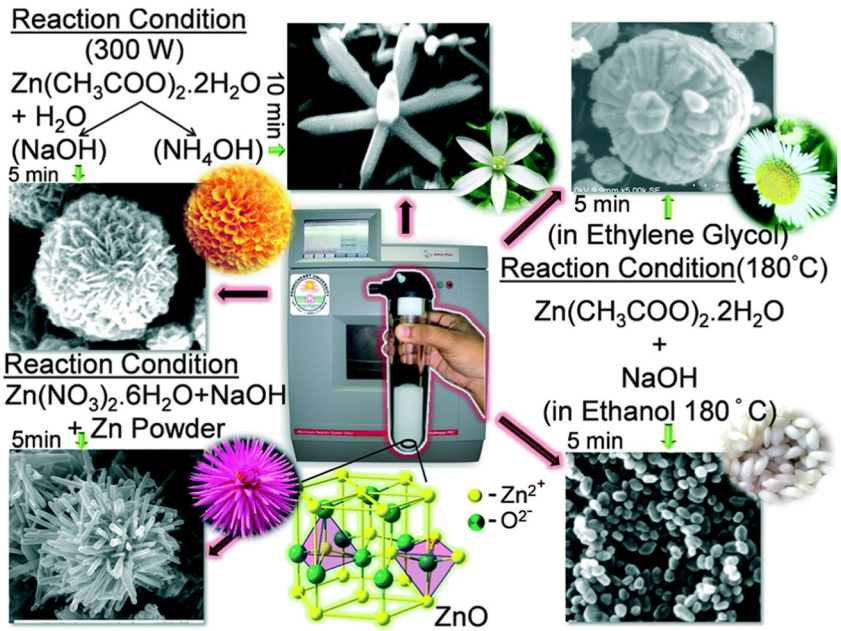

Fig. 9 Several morphologies of ZnO (flower-like marigold, multipod jasmine flower-like, sea urchin-rod flower like, calendula flower-like, and rice grain shape-like) obtained by MAH/S method by changing the zinc source and solvents. Reproduced with permission from Ref. [78], Copyright (2015) The Royal Society of Chemistry

generated. Meanwhile, employing octanol as solvent with $TiCl_4$, resulted into the tetragonal rutile phase while tetragonal anatase with a small quantity of tetragonal rutile were obtained with $TiCl_3$. A change in the morphology followed the change in crystalline phase of TiO_2. The influence of reaction time was also investigated by Moura et al. [128]. They found that 1 min was sufficient to produce coalescence and misshaped spheres of TiO_2. The sphere shape was preserved until 30 min of reaction; however, after 60 min, rods also appeared to be mixed with the spheres.

4.3 P-type metal oxide semiconductors

Many p-type MOS have been synthesized by MAH/S method, including Cu_2O [129], Cr_2O_3 [130], CoO [130, 131], Mn_2O_3 [130, 132], Mn_3O_4 [131], and MnO_x (with Mn_3O_4 as principal component) [133]. However, we focused only on four metal oxides: CuO, NiO, Co_3O_4, and Bi_2O_3, discussing their synthesis in more detail. Figure 10 illustrates the morphology of such materials, for example NiO flakes [134], Co_3O_4 nanocubes [135], and Bi_2O_3 needles [136].

4.3.1 CuO

Different morphologies of CuO were obtained by changing the copper source at the same synthesis conditions. For example, the use of $Cu(CH_3COO)_2$ or $Cu(NO_3)_2$ resulted in spherical particles or flower-like rod morphologies, respectively. The change in morphology also changed the catalytic activity, which was higher for the spheres [137]. Volanti and co-workers [69] demonstrated the stages involved in the formation of CuO with sea urchin-like morphology. In the first steps, a heterogeneous nucleation was promoted by hollow nanospheres; then the particles began to form triangular plates while they grew and sharp points became evident in the cores. These cores transformed into cross-like structures and lastly, 3D structures became evident with an open structure, which began to close until the sea urchin-like morphology was obtained with the growth of the plates over time. The whole process of formation of CuO urchin-like is seen in Fig. 11.

Three distinct morphologies of CuO were prepared by changing the solvent or base in the synthesis. The urchin-like morphology was obtained using $CuCl_2$ and NH_4OH in aqueous medium, whereas the use of NaOH instead of NH_4OH or ethanol instead of water changed the morphology to fiber-like and nanorod-like, respectively. The CuO urchin-like structures showed a superior catalytic activity for the catalytic dehydrogenation of ethanol in acetaldehyde [138].

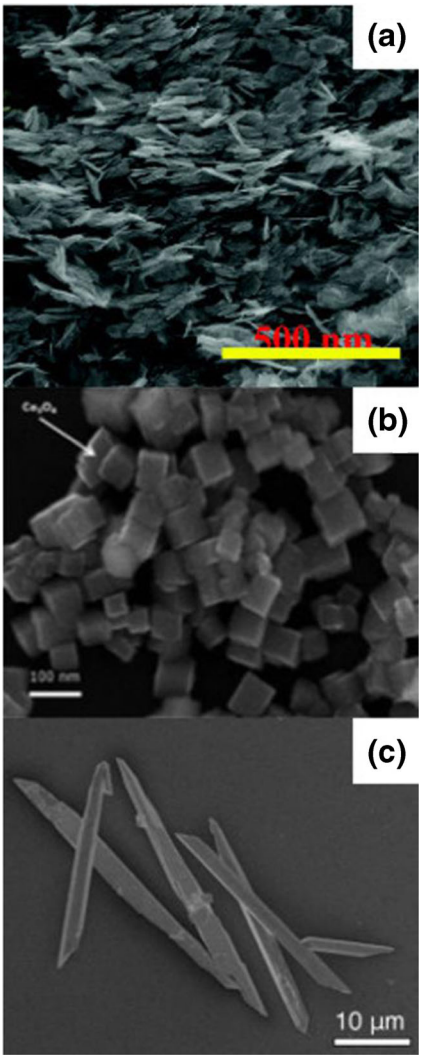

Fig. 10 SEM images of (**a**) Flake shaped NiO prepared using 600 W of microwave power for 1 min. Adapted with permission from Ref. [134], Copyright (2015) The Royal Society of Chemistry; (**b**) Co_3O_4 nanocubes synthesized at 140 °C for 1 h. Adapted with permission from Ref. [135], Copyright (2013) The Royal Society of Chemistry; (**c**) needle-like morphology of α-Bi_2O_3 without pressure-assisted heat treatment. Adapted with permission from Ref. [136], Copyright (2015) American Chemical Society

4.3.2 NiO

NiO with nanoflake-like morphology has been produced for supercapacitor applications. The nanoflakes were synthesized by first preparing β-$Ni(OH)_2$ by MAH followed by calcination at 300, 400 and 500 °C. Nanoflake-like hexagonal β-$Ni(OH)_2$ was obtained after 5 min of microwave treatment, using $Ni(NO_3)_2.6H_2O$, cetyltrimethyl ammonium bromide (CTAB) and ammonia. The calcination of β-$Ni(OH)_2$ at 300 °C resulted to the formation of cubic NiO while preserving the nanoflake morphology. This phase exhibited the most promising results for supercapacitor applications, with

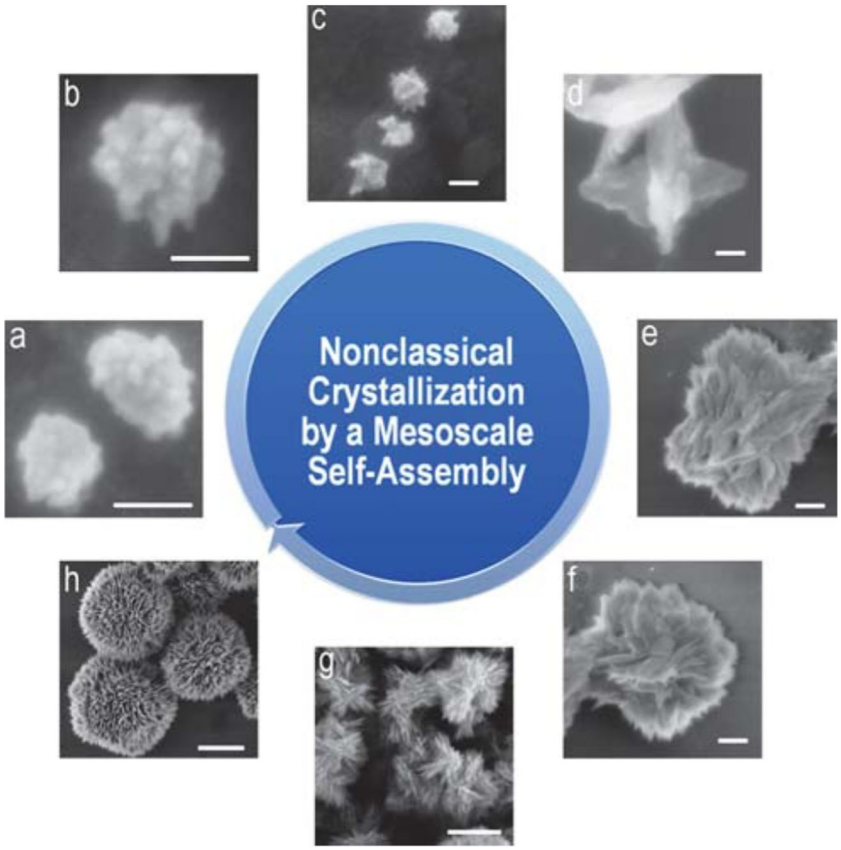

Fig. 11 Stages of formation of CuO sea urchin-like synthesized by MAH method. (**a**) First CuO nanoparticle cores, (**b**–**c**) initial triangular points, (**d**) begin of the self-assembly process of CuO, (**e**–**f**) flower-like structures, (**g**–**h**) final 3D CuO sea urchin-like structure. Scale bars: (a–d) 60 nm; (e–f) 200 nm and (g–h) 1 mm. Reproduced with permission from Ref. [69], Copyright (2010) The Royal Society of Chemistry

maximum specific capacitance of 401 F g^{-1} at current density of 0.5 mA cm^{-2} [100].

Alternative preparation of NiO nanoflakes was reported by Babu and co-workers [134]. In this case, synthesis was performed by the reaction of $Ni(NO_3)_2.6H_2O$ and ammonia in the absence of surfactant, using a different range of microwave radiation intensities (300–900 W). Higher microwave power, 600 and 900 W, was demonstrated to result in well-defined flake-like morphology with low agglomeration. The flake shaped NiO produced with 600 W are shown in Fig. 10(a). These NiO samples exhibited enhanced specific capacitance.

4.3.3 Co_3O_4

Co_3O_4 nanocubes, with a lateral size of 20 nm, prepared by the microwave-assisted solvothermal method for 20 min, were used as gas sensors for detection of xylene and ethanol [139]. Chen et al. [140] demonstrated that MAH synthesis of Co_3O_4 with subsequent annealing promoted the formation of mesoporous nanoflakes. This mesoporous structure led to efficient catalysis of oxygen evolution as well as the catalytic stability of Co_3O_4.

Mulinari et al. [135] discussed the growth process of the crystalline Co_3O_4 nanocubes by MAH synthesis carried out for 10, 30 and 60 min at 140 °C in aqueous medium. Increasing the reaction time resulted into decreasing the poor crystallinity of the β-$Co(OH)_2$ phase, while high crystalline nanocubes of Co_3O_4 became more evident. Figure 10(b) shows the nanocube morphology of Co_3O_4. The process could be explained by the two following steps: first, hydrolysis of cobalt salt used as precursor, leading to the formation of β-$Co(OH)_2$; second, fast heating promoted the nucleation, dissolution and recrystallization for transforming β-$Co(OH)_2$ into Co_3O_4.

4.3.4 Bi_2O_3

The photoluminescent property of α-Bi_2O_3 needles was evaluated for two different samples: the first was obtained by MAH synthesis (Fig. 10(c)), and the second by pressure-assisted heat treatment following MAH. The pressure treatment was found to enhance the angle between $[BiO_6]$-$[BiO_6]$ clusters, promoting an increase in the material's electronic density, which led to higher photoluminescence emission intensity. Theoretical studies were carried out to further understand the observed photoluminescence properties [136]. Liu et al. [141] reported the MAH preparation of cubic γ-Bi_2O_3 with nanorod

structure, as well as the composite with reduced graphene oxide. The photocatalytic performance for both materials was evaluated, with degradation of methyl orange reported to be 78% for pure Bi_2O_3 vs 93% for the composite after 240 min under visible light.

4.4 Electroceramics

The preparation of electroceramics, by the MAH process including $BaTiO_3$, $SrTiO_3$, $Sr_{0.5}Ba_{0.5}TiO_3$, $PbTiO_3$, $Pb(Zr_{0.52}Ti_{0.48})O_3$, $SrZrO_3$, $BaZrO_3$, as well as pyrochlore phases with the $Pb(Mg_{1/3}Nb_{2/3})O_3$ and $Pb(Zn_{1/3}Nb_{2/3})O_3$ compositions, were first highlighted by the Komarneni group [7]. The number of electroceramic materials prepared by MAH/S has continued to increase. The syntheses of different electroceramics have recently been reported, including $Ba_{1-x}Ca_xTiO_3$ [142], $BiFeO_3$ [143], and $BiFe_xCr_{1-x}O_3$ [144]. Figure 12 gives some examples of morphologies achieved in the MAH/S synthesis of $BaTiO_3$, $CaTiO_3$, and $BaZrO_3$. The process of obtaining each of these materials will be further detailed in the following sections.

4.4.1 $BaTiO_3$

Different reaction conditions have been applied to produce barium titanate ($BaTiO_3$) using the MAH method. Swaminathan et al. [145] studied the effect of MW irradiation time on $BaTiO_3$ synthesis. They demonstrated a polymorphic change from cubic, for lower reaction times, to tetragonal structure after 15 min of MW irradiation. For longer reaction times, the nanocube morphology was preserved, but with increased particle size. Figure 12(a) shows the morphology of $BaTiO_3$ produced within 15 min of MW irradiation. Moreira et al. [42] also studied the time dependence of $BaTiO_3$ nanoparticle using MAH synthesis. They found that the tetragonal structure as well as the spherical morphology persisted for all reaction times.

4.4.2 $CaTiO_3$

Rectangular $CaTiO_3$ particles were obtained by the MAH route using TiO_2, $CaCl_2$, urea and NaOH as reactants. The urea played an important role of shape-controlling, leading to rectangular prism-like morphology, as shown in the SEM image in Fig. 12(b) [146]. Mazzo et al. [147] verified the effect of two titanium precursors (titanium tetrachloride and titanium tetraisopropoxide) on the synthesis of $CaTiO_3$. Micro-cube morphology was obtained for both precursors, but with the use of titanium tetraisopropoxide, $CaCO_3$ impurity was detected and the material was found to be less crystalline. The mechanism of self-assembly of nanoplates was proposed for the formation of the cube-shape morphology.

4.4.3 $BaZrO_3$

The process of $BaZrO_3$ decaoctahedron growth was studied in detail by Moreira et al. [148]. In the early stages of the reaction (10 min), spherical-like structures were obtained, however $BaCO_3$ and ZrO_2 as secondary phases were still present. At 20 min, a pseudo core-shell morphology was obtained and the gradual growth of polyhedral was observed with longer times of reaction (> 40 min.). The SEM image in Fig. 12(c) highlights the decaoctahedron shape of $BaZrO_3$ synthesized for 40 min. In each of these different stages of growth, the mechanisms of oriented attachment and Ostwald ripening were described. De Keukeleere et al. [149] studied the difference between microwave-assisted and conventional solvothermal /hydrothermal synthesis of $BaZrO_3$ nanoparticles. For hydrothermal conditions, both methods resulted into mainly amorphous material, that required further heating at 700 °C. On the other hand, the microwave-assisted solvothermal (using water and isopropanol as solvents) synthesis led to the formation of crystalline $BaZrO_3$ nanoparticles in a lower reaction time compared to the conventional solvothermal method.

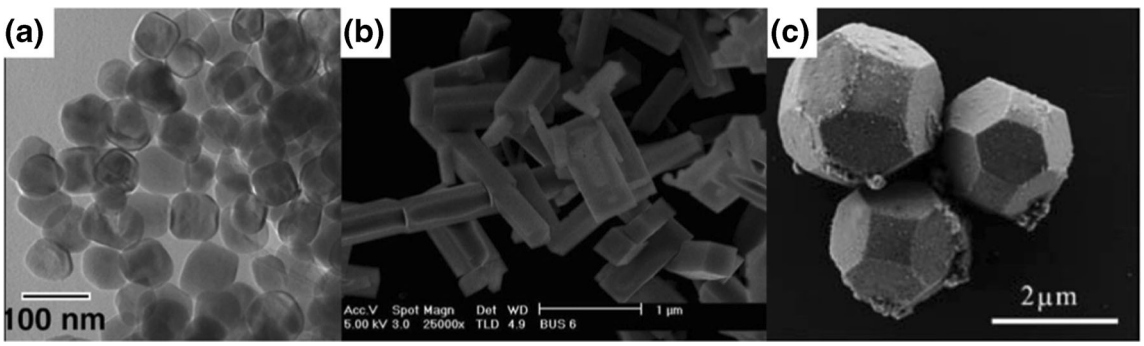

Fig. 12 (**a**) TEM image of $BaTiO_3$ nanocubes prepared with 15 min of MW irradiation. Adapted with permission from Ref. [145], Copyright (2010) American Chemical Society. SEM images of: (**b**) $CaTiO_3$ with box-shaped rectangular morphology. Adapted with permission from Ref. [146], Copyright (2013) The Royal Society of Chemistry; (**c**) $BaZrO_3$ decaoctahedron obtained in 40 min of MAH treatment. Adapted with permission from Ref. [147], Copyright (2011) The Royal Society of Chemistry

4.5 Graphene

Graphene has attracted great interest due to its unique characteristics. MW has been used to synthesize graphene [150], to reduce graphene oxide (GO) to graphene or reduced graphene oxide (RGO) [151–154], and to prepare composites of metal oxides and graphene, discussed latter. Hu et al. [152] studied the capacity of microwave absorption by graphite oxide based on its degree of oxygenation, showing that the less oxidized samples interacted more with microwave radiation reaching higher temperatures. As a result, when a mixture of graphene and GO was irradiated by MW, the MW energy was transformed to heat, allowing the reduction of adjacent GO to graphene (Fig. 13).

Microwave irradiation at a temperature range between 120 and 200 °C was used to prepare graphene sheets from expanded graphite using aqueous ammonia solution [150]. Ammonia plays the role of fabricating a more reduced graphene, since the synthesis carried out in pure water resulted in a high amount of oxygenated groups.

4.6 Composite materials

In this section, we exemplify three kinds of composite materials: n-p junction, metal-metal oxide semiconductor, and graphene-metal oxide semiconductor. Figure 14(a) shows a high resolution TEM image of an n-p junction, in which the heterojunction between p-type CuO and n-type TiO_2 can be visualized through the lattice fringes of CuO and TiO_2 polymorphs (anatase and rutile) [155]; see section 4.6.1 for a more detailed description of the CuO/TiO_2 heterojunction. The TEM image in Fig. 14(b) shows the distribution of gold nanoparticles on the surface and in the framework of hollow ZnO nano-doughnuts, forming ZnO/Au nanocomposites [156] (section 4.6.2). A composite of In_2O_3-RGO synthesized using indium nitride and GO by MAH method [157] is shown in Fig. 14(c). The distribution of well-faceted In_2O_3 nanocubes on graphene sheets can be seen, generating a transparent film.

4.6.1 n-p junctions

Huang et al. [158] reported the synthesis of Bi_2O_3/Bi_2WO_6 heterostructures. They showed that at synthesis temperature of 180 °C only the orthorhombic phase of Bi_2WO_6 was obtained, while increasing the temperature enabled formation of higher content of cubic Bi_2O_3. Thus, a p-n junction of p-type Bi_2O_3 and n-type Bi_2WO_6 could be generated. NH_4F was also used in the synthesis, fluoride ions could enter the Bi_2WO_6 lattice, resulting to formation of a $Bi_2O_3/Bi_2WO_{6-x}F_{2x}$ heterostructure. The analysis showed that the p-n junction promoted higher photocatalytic activity with respect to photodegradation of rhodamine B.

The p-type-CuO/n-type-TiO_2 heterojunction used for photocatalytic degradation of 2,4-dichlorophenoxyacetic acid was also reported [155]. The heterostructure was prepared from a mixture of TiO_2 and $Cu(CO_2CH_3)_2.H_2O$ in ethanol, heated under MAH treatment for 5 min at 150 °C. The formation of CuO particles was attributed to the $Cu(OH)_2$ species, and a homogeneous dispersion of CuO promoted by the microwave method was demonstrated.

4.6.2 Metal-metal oxide junctions

The preparations of different junctions of metal and metal oxide by the microwave-assisted method have been reported in a series of studies. Rai et al. [159] described the synthesis of core-shell $Ag@SnO_2$ nanoparticles (NPs), in which the Ag NPs were first prepared by the colloidal method, followed by deposition of SnO_2 NPs on Ag NPs by the MAH method. The MAH treatment resulted in an excellent dispersion of $Ag@SnO_2$ NPs, with no isolated Ag NPs in the sample. Moreover, the Ag surface plasmon was red-shifted after the SnO_2 shell formation. Finally, it was discovered that the presence of Ag NPs improved the gas sensing detection of SnO_2 for p-xylene.

Cu/Cu_2O heterostructures were prepared by the MAH method, in which the change of reaction time led to different

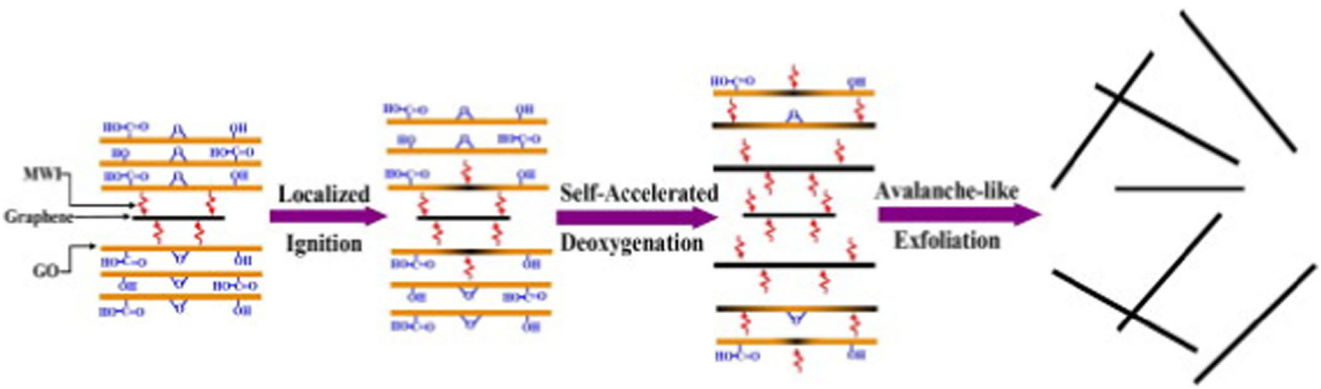

Fig. 13 Process of graphene formation: first, the graphene absorbs microwave irradiation and ignites, then an avalanche-like process of deoxygenation of GO occurs, leading to the formation of graphene. Reproduced with permission from Ref. [152], Copyright (2012) Elsevier

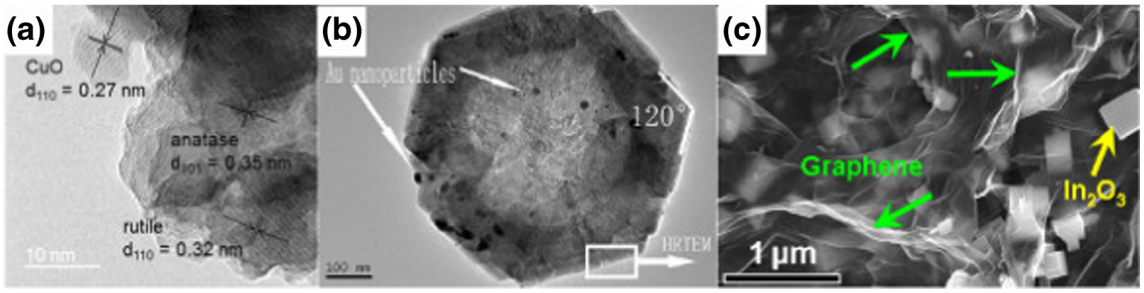

Fig. 14 (**a**) High resolution TEM image of CuO/TiO_2 junction, showing the lattice spacings of CuO and TiO_2. Adapted with permission from Ref. [155], Copyright (2015) Wiley-VCH; (**b**) TEM image of hollow doughnut-like Au/ZnO nanocomposites. Adapted with permission from Ref. [156], Copyright (2012) American Chemical Society; (**c**) SEM image of In_2O_3 cube/RGO composites. Adapted with permission from Ref. [157], Copyright (2014) American Chemical Society

morphologies and the amount of Cu in the heterostructure increased with longer times. Obtaining Cu/Cu_2O in a single-step was possible due to the reduction of Cu_2O by ascorbic acid during synthesis. The hollow sphere obtained in 30 min of synthesis, which contained 10.5% wt of Cu, exhibited the highest photocatalytic degradation activity as well as the best gas sensing performance compared with the heterostructures synthesized with 5, 10, 20 and 60 min [76].

Geng et al. [156] reported the synthesis of hollow doughnut-like ZnO/Au by the one-step MAH method. Here, the formation of ZnO and reduction of Au occurred simultaneously, resulting to a dispersion of Au nanoparticles on the surface and in the structure of ZnO. This nanocomposite exhibited good biocompatibility, showing one more potential application for these materials.

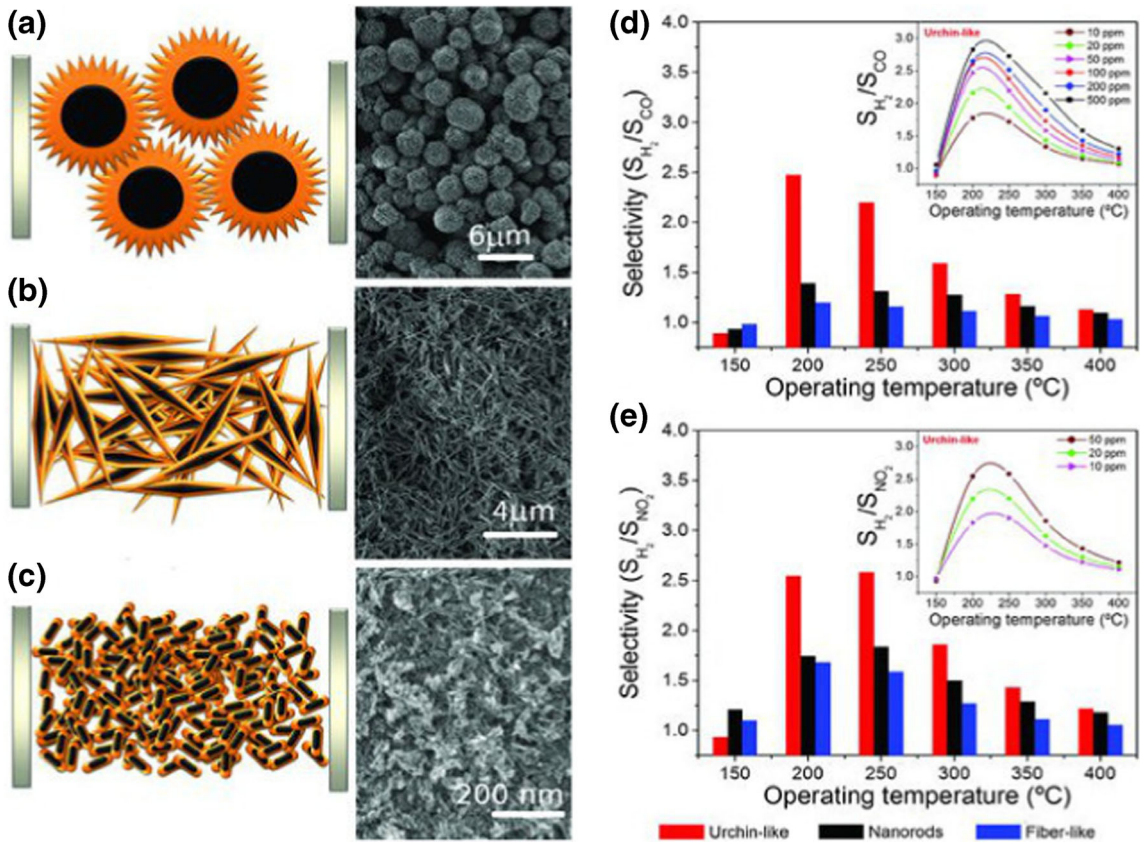

Fig. 15 (Left) Schematics of CuO particle-particle contacts and the SEM images for (**a**) urchin-like, (**b**) fiber-like, and (**c**) nanorods morphologies. The black and the orange regions correspond to bulk resistance and Debye-layer, respectively, while the gray region corresponds to the electrical contact. (Right) The selectivity for 50 ppm H_2 in relation to CO (**d**) and (**e**) NO_2 as function of temperature for the three CuO morphologies. The insets indicate the selectivity as function of operating temperatures for different gas concentration for CuO urchin-like structure. Adapted with permission from Ref. [187], Copyright (2012) Wiley-VCH

4.6.3 Graphene-metal oxide junctions

The synthesis of composites of metal oxides and graphene (or graphene-based materials) by MAH has been extensively studied. Composites of graphene or RGO with SnO_2 [74, 160–162], In_2O_3 [157], Mn_3O_4 [163, 164], TiO_2 [165], CuO [166–168], Cu_2O [14], Co_3O_4 [169], Fe_2O_3 [170], ZnO [171, 172], and WO_3 [173, 174] have been reported.

Zhong et al. [161] developed rapid synthesis (20 min) of sandwiched SnO_2 nanoparticles between graphene sheets by the microwave autoclave method. This method consisted of a two-step process: the first step involves the formation of SnO_2 nanoparticles onto the graphite oxide, followed by reduction of graphite oxide to graphene as the second step. This method resulted in well dispersed SnO_2 nanoparticles on graphene nanosheets, preventing restacking of the graphene sheets. The synthesis of RGO-SnO_2 nanocomposites by a one-pot MAS method was also reported by Zito et al. [175]. The one-step method allowed the graphene oxide reduction and the growth of hollow SnO_2 nanoparticles to occur concomitantly, as well it promoted a greater interconnectivity between RGO and SnO_2. The evaluation of the gas sensing performance revealed that the nanocomposite exhibited a high ethanol response, which was larger than the response of pure hollow SnO_2 nanoparticles, indicating the role of RGO in the gas-sensing performance.

Zhou et al. [166] reported a facile and rapid single-step MAH synthesis of graphene-wrapped CuO spheres. Samples with different content of CuO were studied with the graphene wrapped CuO spheres preventing their aggregation, with the material containing 16.9% of graphene showing the best electrochemical performance.

Hydrophobic ZnO nanoparticles were anchored onto graphene sheets by MAH at 160 °C, followed by annealing at 100 °C in order to transform $Zn(OH)_2$ into ZnO. The hydrophobic character of ZnO nanoparticles allowed their dispersion on graphene sheets without chemical modification. This characteristic makes it desirable for solar cells application, since the hydrophobic ZnO-graphene nanocomposite

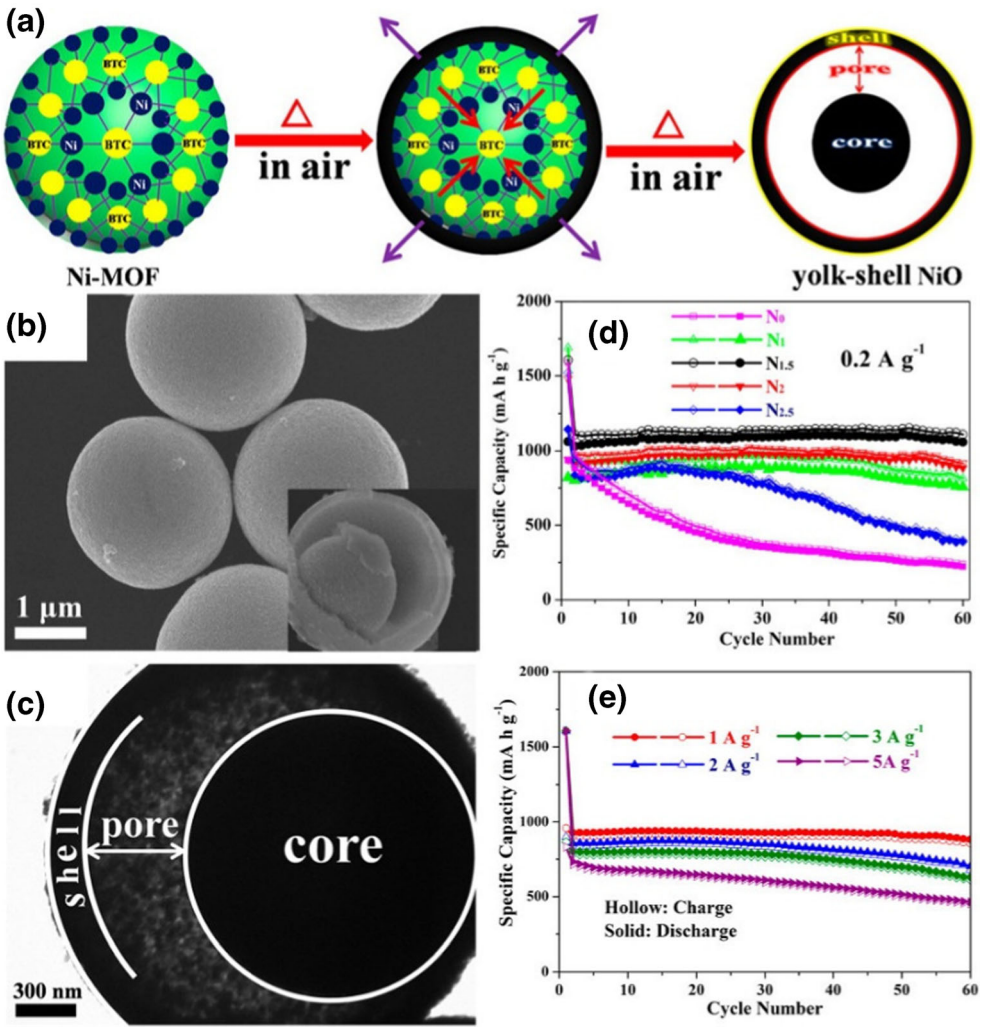

Fig. 16 (**a**) Formation of yolk–shell NiO Microspheres starting from MAH Synthesis of Ni-based Metal–Organic Framework; (**b**) SEM images of NiO microsphere ($N_{1.5}$); (**c**) TEM image of NiO microsphere ($N_{1.5}$); (**d**) Cycling performances of different NiO structures (N_0, N_1, $N_{1.5}$, N_2, and $N_{2.5}$) at 0.2 A g^{-1}; (**e**) Cycling performances of the yolk–shell NiO of $N_{1.5}$ at different current densities. Adapted with permission from Ref. [188], Copyright (2015) American Chemical Society

could be mixed with polymer-fullerene blend (PCPDTBT:PCBM), thus improving the solar cell performance through better charge transport [171].

5 Applications of materials synthetized by MW-assisted hydrothermal/solvothermal method

5.1 Gas sensors

A growing number of materials synthesized by the microwave hydrothermal/solvothermal method are being examined for gas sensor applications. ZnO [176], WO_3 [177], and In_2O_3-graphene [157] were used for NO_2 detection; Pd/SnO_2 [178], Au@TiO_2 [179], and Au/SnO_2 [180] for CO sensing; TiO_2 [181], and Pd-GO [182] as H_2 gas sensors; and α-Fe_2O_3/SnO_2 [183], CuO [184, 185], and ZnO [120] for ethanol detection. Ag@SnO_2 core-shell nanoparticles obtained by MAH method exhibited a higher gas sensor response for p-xylene compared to pure SnO_2, showing that Ag NPs play an important role in the sensing mechanism due to their electronic and catalytic activity. The transformation of p-xylene into more active species by Ag NP catalyst after gas diffusion through SnO_2 shells explained the improvement in Ag@SnO_2 selectivity [158].

Hierarchical flower-like SnO_2 structures were also applied as efficient ethanol sensors [186]. These structures exhibited excellent sensing properties that were attributed to the unique hierarchical morphology, facilitating the gas diffusion, but also to the surface defects and the high specific surface area promoted by the MAS method.

Volanti et al. [187] examined the influence of CuO morphology on H_2 gas sensing performance. All three samples (urchin-like, fiber-like, and nanorods) exhibited good selectivity for H_2 compared to CO and NO_2 at different temperatures. However, at 200 °C, the H_2 sensitivity of urchin-like specimens presented enhanced sensor signal compared to the other morphologies. The unique morphology of urchins providing parallel particle-particle contacts explained the better sensor response obtained for this material. Figure 15 gives an overview of the H_2 selectivity of the gas sensor based on CuO with different morphologies.

The combination of Cu_2O nanorods and RGO led to a composite with remarkable response to NH_3 at room temperature. The RGO was shown to play an important role in gas detection, since Cu_2O by itself exhibited weak response even to 1000 ppm NH_3 at elevated temperature (270 °C), whereas the Cu_2O-RGO composites detected 100 ppm NH_3 at room temperature. Furthermore, the composite sensor exhibited higher selectivity for NH_3 with excellent repeatability [14].

5.2 Batteries

SnO_2-RGO composites with graphene content of 33.3 wt% showed enhanced Li-cycling performance compared to pure SnO_2, attributed to the graphene preserving the structural integrity of the composite. The cycling behavior study revealed that SnO_2-RGO had a reversible discharge capacity of 590 mA h g^{-1} for up to 200 cycles, whereas for pure SnO_2 this value only reached 78 mA h g^{-1} [161].

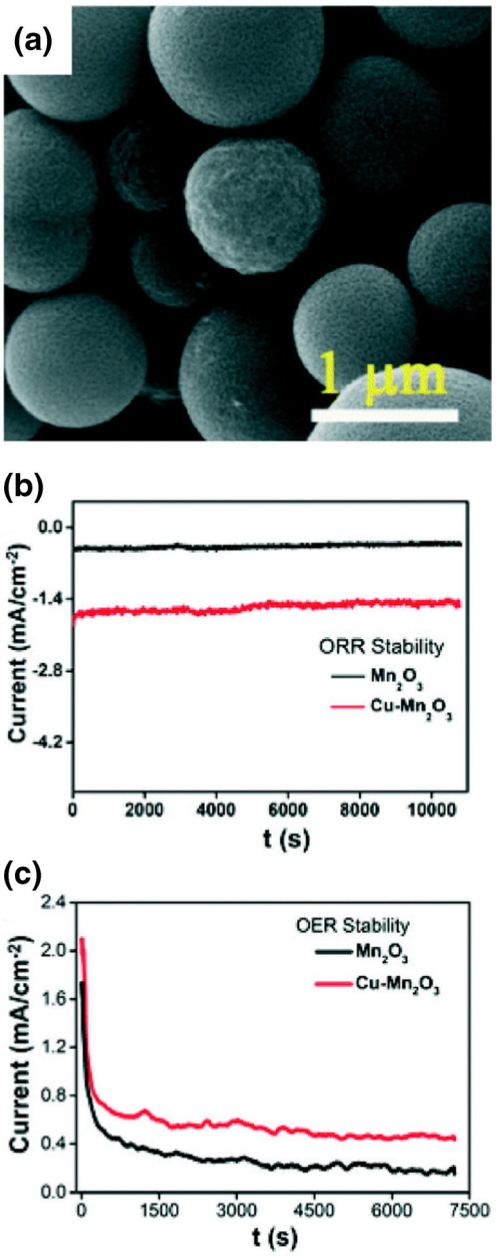

Fig. 17 (**a**) SEM image of Cu-Mn_2O_3 nanoballs. Chronoamperometric curves for the: (**b**) oxygen reduction reaction, (**c**) oxygen evolution reaction, showing distinct long-term choronoamperometic stability. Adapted with permission from Ref. [190], Copyright (2015) The Royal Society of Chemistry

Lu and Wang [166] reported the growth of two different morphologies of CuO, nanosheets and *fusiform*, on graphene sheets, which was achieved by changing the reaction temperature. Both hybrid materials exhibited superior lithium-storage capacity than pure CuO and graphene because their layer-by-layer structure is likely to contain extra micro-pores and defects for Li storage. After 40 cycles, the charge capacities of the CuO nanosheets-graphene and fusiform CuO-graphene were 801 and 666 mA h g^{-1}, respectively, while for pristine CuO and graphene these values were 173 and 631 mA h g^{-1}.

Kong et al. [188] produced yolk-shell NiO nanospheres by synthesis of Ni-based metal-organic frameworks (Ni-MOF) using the MAH method, followed by calcination at 500 °C, seen in Fig. 16(a). This method produced a material with mesoporous structure (Fig. 16(b–c)), which was the reason for the large charge capacity of 1063 mA h g^{-1}, at a current density of 0.2 A g^{-1}. Moreover, the charge capacity of yolk-shell NiO nanospheres showed negligible decrease to 1060 mA h g^{-1} after 60 cycles (Fig. 16(d)). At larger current densities, the nanospheres showed lower charge capacity and more rapid capacity fading (Fig. 16(e)). The acronym $N_{1.5}$ in the figures refers to the molar ratio $Ni(NO_3)_2$:benzene-1,3,5-tricarboxylic acid (BTC) equal to 1.5, which was the optimal ratio to obtain the yolk-shell NiO nanospheres.

5.3 Fuel cells

Chen et al. [189] prepared carbon supported Pt nanoparticles (Pt/C) using microwave irradiation and compared it with a commercial Pt/C catalyst. They demonstrated that Pt/C prepared by microwave irradiation showed a higher electrocatalytic performance for electrooxidation of methanol at room temperature. This result was mainly attributed to the uniformity of the small Pt particles, which was possible due to the microwave treatment. Mn_2O_3 and Cu-doped Mn_2O_3 nanoballs, as seen in Fig. 17(a), were synthesized by MAH and their potential as catalysts for alkaline fuel cells was also studied [190]. Both materials (Cu-doped and pure Mn_2O_3) exhibited great stability for oxygen reduction and evolution reaction in alkaline medium, evaluated by chronoamperometry (Fig. 17(b–c)). The materials showed distinct long-term choronoamperometic stability, necessary for alkaline fuel cells. In addition, the Cu presence improved the electrocatalytic activity.

5.4 Photocatalysis

ZnS@ZnO core-shell structures, prepared in one-step process, were shown to exhibit increased photocatalytic activity for p-chlorophenol compared to pure ZnO or ZnS. Moreover, no crystallographic phase change was observed after the photocatalytic reaction. Furthermore, photocorrosion observed for pure ZnO was overcome, showing good stability as photocatalyst [89]. Different morphologies of ZnO (plates, rounded plates, brush-like, and 3-D flower-like) were prepared by MAH/S method, changing the precursor concentration, reaction time, temperature, and solvent [191]. The photocatalytic activity was studied under UV and visible illumination. The rounded plates and flower-like structures

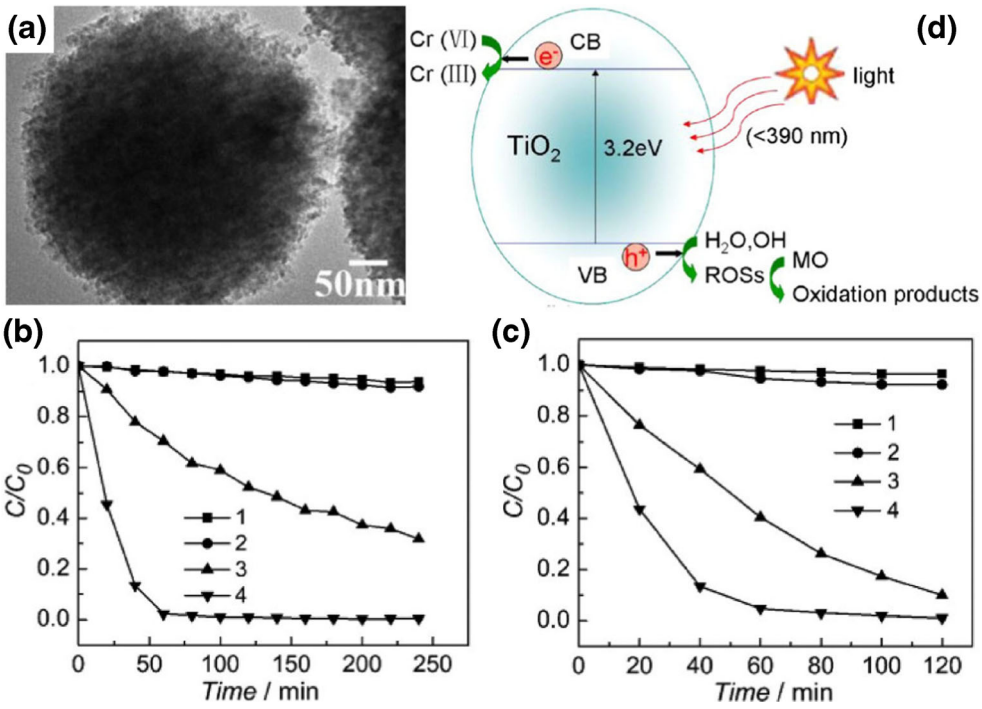

Fig. 18 (**a**) TEM image of TiO_2 showing the pores of the microsphere. Conversion of (**b**) Cr(VI) and (**c**) methyl orange. C_0 is the original concentration of Cr(VI) or methyl orange, C is concentration of the remaining Cr(VI) or methyl orange at a specific time t. Curve 1– the photocatalyst is absent in the single systems, 2- photocatalyst is absent in the mixed system with Cr(VI) and methyl orange, 3- TiO_2 in the Cr(VI) or methyl orange single system, 4- TiO_2 in the mixed system of Cr(VI) and methyl orange, respectively. (**d**) Conversion mechanism of Cr(VI) and methyl orange by TiO_2 under UV light irradiation, in which ROSs are the reactive oxidative species. Adapted with permission from Ref. [126], Copyright (2014) American Chemical Society

presented enhanced photocatalytic activity, which was related to the oxygen vacancies created in the crystal growth process.

Yang et al. [126] demonstrated the photocatalytic efficiency of nanoparticulate TiO_2 microspheres synthesized by MAH. Figure 18(a) shows the porosity of the microspheres. When the photocatalyst was applied for the decontamination of a mixture of Cr(VI) with methyl orange, higher reduction of Cr(VI) and oxidation of methyl orange was observed (Fig. 18(b–c), curve 4), while for pure Cr(VI) or methyl orange the efficiency was not so enhanced (Fig. 18(b–c), curve 3). In addition to this synergistic effect, the photocatalyst could be easily recovered with its efficiency nearly constant after 3 cycles. Figure 18(d) illustrates the synergistic effect of reduction of Cr(VI) with the simultaneous oxidation of methyl orange.

Cu/Cu_2O hollow spheres demonstrated good photocatalytic activity because of their porous structure and heterojunctions. In 30 min, 92.1% of methyl orange was degraded. However, after the third cycle, a decrease of 23% in photocatalytic activity was reported, attributed to the photooxidation to CuO [76].

5.5 Solar cells

TiO_2 nanorods were grown on substrates of fluorine-doped tin oxide (FTO) by MAH. Figure 19(a) displays the TEM image of a typical TiO_2 nanorod. The FTO substrates were coated with a thin layer of TiO_2 nanoparticles, which helped to promote heterogeneous nucleation of the nanorods. Following synthesis, the nanorods were also immersed in $TiCl_4$ solution. The results showed an energy conversion efficiency of 1.31% for the TiO_2 based dye-sensitized solar cell (DSSC) without $TiCl_4$ treatment, while after treatment with $TiCl_4$ for 2 h, this value increased to 3.7%, probably due to the quantity of dye adsorbed on the coating layer. Furthermore, the diffusion coefficient and carrier life time of DSSCs were analyzed and it was found that increasing the treatment time with TCl_4, the diffusion coefficient decreased (Fig. 19(b)), but the lifetime remained unchanged except for the nanorod without treatment (Fig. 19(c)), which was attributed to the backward electron transfer from the FTO to the electrolyte [192].

Liu et al. [193] described synthesis of ZnO nanowire arrays on FTO substrates by MAH from 1 to 5 h. With increasing reaction time, the length of the nanowires increased from 3.4 to 17.2 μm, which led to the increase of internal surface area along the enhancement of the energy conversion efficiency when the ZnO nanowires were used as DSSC photoanodes. The lowest efficiency was obtained (0.35%) for ZnO nanowires with length of 3.4 μm, whereas maximum efficiency of 1.25% was achieved for nanowires of 17.2 μm, due to the

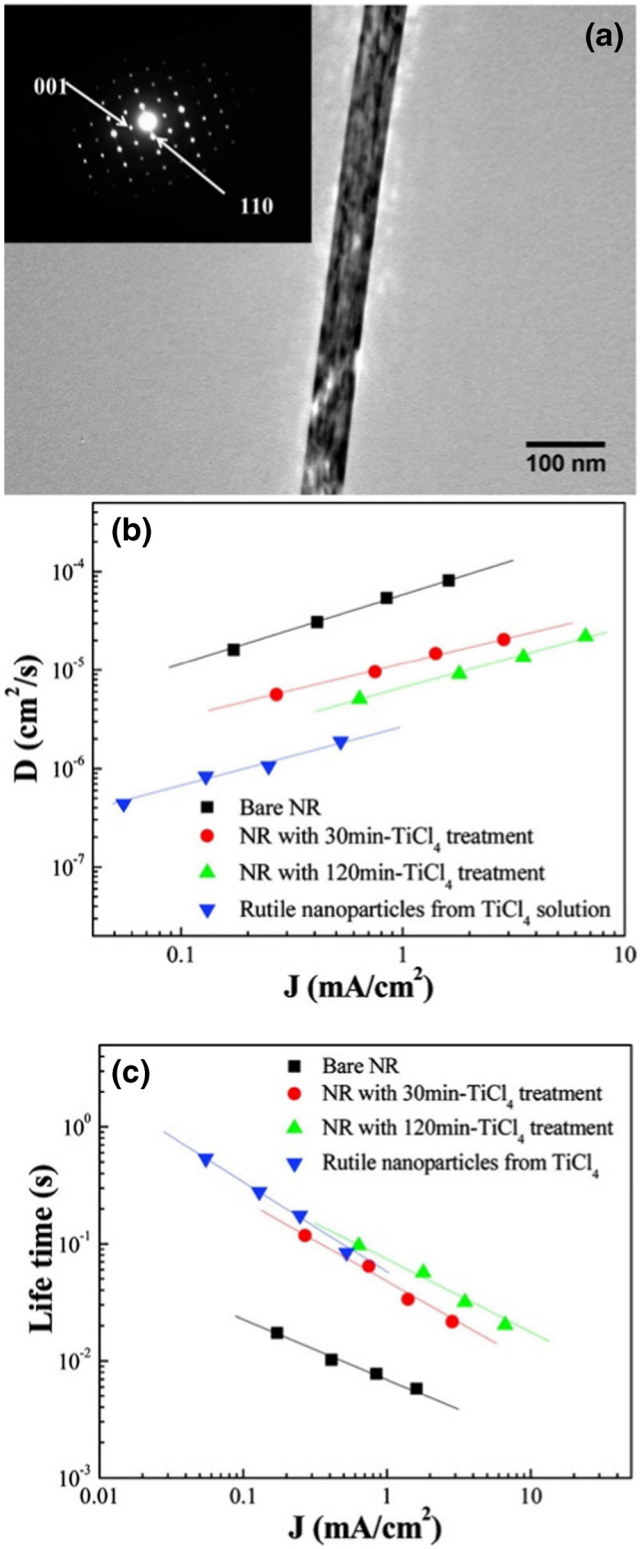

Fig. 19 (**a**) TEM image of TiO_2 nanorod, and the selected area diffraction pattern in the inset. (**b**) Diffusion coefficient and (**c**) lifetime of DSSCs for pure nanorods, nanorods treated with $TiCl_4$ for different times, rutile nanoparticles grown from $TiCl_4$ solution. Adapted with permission from Ref. [192], Copyright (2011) American Chemical Society

highest quantity of dye absorbed on the ZnO as a result of the larger internal surface area of the array.

Four distinct morphologies of SnO_2 were obtained by a microwave-assisted solvothermal process by using four bases NaOH, KOH, TMAOH, and NH_4OH. All these materials were deposited on a FTO substrate, and then tested as photoanodes for DSSC. The energy conversion efficiency was better than 1.5% for all morphologies of SnO_2, except for the one prepared with TMAOH which exhibited the highest efficiency of 3.6%. In addition, the four samples of SnO_2 photoanodes showed an enhanced efficiency during the first 15 days, and after which the efficiency remained unchanged for up to 50 days [194].

6 Conclusions and outlook

This work provided an overview of MAH/S discussing microwave heating theory and means for achieving fine crystal morphology control. This method holds great promise for the preparation of different classes of materials such as metals, semiconductors, electroceramics, composites, etc. from solution via nucleation/growth mechanisms for technological applications relevant to advanced gas sensors, batteries, fuel cells, photocatalysts, and solar cells. Some research trends and directions are expected including: (1) achieving a detailed understanding of crystal shape by chemical reaction, nucleation, and growth of inorganic, organic or composite materials in liquid phase under microwave irradiation; (2) clarifying controversial non-thermal or specific microwave effects under microwave irradiation; (3) generating theoretical simulations of microwave effects in crystal morphology modeling; (4) developing sustainable, clean and green microwave-assisted synthesis methods at low cost and high efficiency; and (5) studying the correlations between structure–property relations and new advanced applications of microwave-prepared nanostructured materials. The major challenges of this method are in interfacing ultrasound, spray pyrolysis, in flow systems especially on scaling-up for industrial applications. Progress towards these goals will greatly advance the MAH/S method and accelerate its practical applications.

Furthermore, the key advantages obtained by the application of MAH/S in materials preparation over conventional conductive heating, specifically are improved higher yields, lower processing time, selective dielectric solvents and/or reagents heating, avoiding direct contact with the MW source, enhanced reproducibility, temperature gradient absence and efficient heating distribution throughout the sample. It was shown that it is possible to obtain porous materials with high surface area that helped decisively in improved application in sensors, catalysts, etc. Also, the control of the size-selective growth assists in the selectivity of these materials. In addition, it is possible to obtain various classes of composites with fine composition which are often difficult to obtain by other synthesis routes. However, the benefits of the use of microwaves in MAH/S remain very broad and deserve to be more explored in the future.

Acknowledgements The authors acknowledge São Paulo Research Foundation (FAPESP), grants #2015/50526-4, #2015/05916-9 and #2014/17343-0; National Council for Scientific and Technological Development – CNPQ, grants #447760/2014-9, #444926/2014-3 and #443138/2016-8, and the Coordination for the Improvement of Higher Education Personnel – CAPES.

References

1. F. Gao, Q.Y. Lu, S. Komarneni, Chem. Mater. **17**, 856 (2005)
2. J. M. Kong, C. V. Wong, Z. Q. Gao, X. T. Chen, Synth. React. Inorganic, Met. Nano-Metal Chem. (2008), pp. 186–188
3. A.M.R. Galletti, C. Antonetti, A.M. Venezia, G. Giambastiani, Appl. Catal. A Gen. **386**, 124 (2010)
4. S.-W. Lee, L.M. Lozano-Sánchez, V. Rodríguez-González, J. Hazard. Mater. **263 Pt 1**, 20 (2013)
5. V. Moghimifar, A. Raisi, A. Aroujalian, N.B. Bandpey, Adv. Mater. Res. **829**, 846 (2013)
6. W. Cao, L. Chen, Z. Qi, J. Mol. Catal. A Chem. **401**, 81 (2015)
7. S. Komarneni, Q. Li, K.M. Stefansson, R. Roy, J. Mater. Res. **8**, 3176 (1993)
8. J.P. Cheng, Mater. Res. Innov. **1**, 44 (1997)
9. S.F. Liu, I.R. Abothu, S. Komarneni, Mater. Lett. **38**, 344 (1999)
10. A. Dias, V.S.T. Ciminelli, Chem. Mater. **15**, 1344 (2003)
11. P. Wan, W. Yang, X. Wang, J. Hu, H. Zhang, Sensors Actuators B Chem. **214**, 36 (2015)
12. S. Bai, C. Chen, R. Luo, A. Chen, D. Li, Sensors Actuators B Chem. **216**, 113 (2015)
13. F. Ren, G. Zhu, P. Ren, K. Wang, X. Cui, X. Yan, Appl. Surf. Sci. **351**, 40 (2015)
14. H. Meng, W. Yang, K. Ding, L. Feng, Y. Guan, J. Mater. Chem. A **3**, 1174 (2015)
15. S. Khamlich, T. Mokrani, M.S. Dhlamini, B.M. Mothudi, M. Maaza, J. Colloid Interface Sci. **461**, 154 (2016)
16. S. Komarneni, Y.D. Noh, J.Y. Kim, S.H. Kim, H. Katsuki, Z. Naturforsch. Sect. B. J. Chem. Sci. **65**, 1033 (2010)
17. F.-H. Ko, Y.-C. Hsu, M.-T. Wang, G.S. Huang, Microelectron. Eng. **84**, 1300 (2007)
18. C.D. Madhusoodana, R.N. Das, Y. Kameshima, K. Okada, J. Mater. Sci. **41**, 1481 (2006)
19. J. Wang, G. Du, R. Zeng, B. Niu, Z. Chen, Z. Guo, S. Dou, Electrochim. Acta **55**, 4805 (2010)
20. R.C. Lima, L.R. Macario, J.W.M. Espinosa, V.M. Longo, R. Erlo, N.L. Marana, J.R. Sambrano, M.L. dos Santos, A.P. Moura, P.S. Pizani, J. Andrés, E. Longo, J.A. Varela, J. Phys. Chem. A **112**, 8970 (2008)
21. D. Zhang, G. Li, X. Yang, and J. C. Yu, Chem. Commun. (Camb). 4381 (2009)
22. M.S. Anwar, S. Kumar, F. Ahmed, G.W. Kim, B.H. Koo, J. Nanosci. Nanotechnol. **12**, 5523 (2012)
23. Z. Zhu, Y. Zhang, Y. Zhang, H. Liu, C. Zhu, Y. Wu, Ceram. Int. **39**, 2567 (2013)

24. D.E. Motaung, G.H. Mhlongo, S.S. Nkosi, G.F. Malgas, B.W. Mwakikunga, E. Coetsee, H.C. Swart, H.M.I. Abdallah, T. Moyo, S.S. Ray, ACS Appl. Mater. Interfaces **6**, 8981 (2014)
25. M. Poupon, N. Barrier, S. Petit, S. Clevers, V. Dupray, Inorg. Chem. **54**, 5660 (2015)
26. L. Wang, Y. Huang, X. Sun, H. Huang, P. Liu, M. Zong, Y. Wang, Nanoscale **6**, 3157 (2014)
27. S.H. Jhung, J.-H. Lee, P.M. Forster, G. Férey, A.K. Cheetham, J.-S. Chang, Chemistry **12**, 7899 (2006)
28. W. Liu, L. Ye, X. Liu, L. Yuan, X. Lu, J. Jiang, Inorg. Chem. Commun. **11**, 1250 (2008)
29. Y. Tian, B. Chen, R. Hua, N. Yu, B. Liu, J. Sun, L. Cheng, H. Zhong, X. Li, J. Zhang, B. Tian, H. Zhong, CrystEngComm **14**, 1760 (2012)
30. J. Huang, C. Xia, L. Cao, X. Zeng, Mater. Sci. Eng. B **150**, 187 (2008)
31. J. Ji, L.L. Zhang, H. Ji, Y. Li, X. Zhao, X. Bai, X. Fan, F. Zhang, R.S. Ruoff, ACS Nano **7**, 6237 (2013)
32. L. Xu, Y.-S. Ding, C.-H. Chen, L. Zhao, C. Rimkus, R. Joesten, S.L. Suib, Chem. Mater. **20**, 308 (2008)
33. Y. Liu, L. Xia, Y. Lu, S. Dai, M. Takeguchi, H. Hong, Z. Pan, J. Colloid Interface Sci. **381**, 24 (2012)
34. C. Yang, F. Xiao, J. Wang, X. Su, Sensors Actuators B Chem. **207**, 177 (2015)
35. C.-Y. Wu, D.S. Raja, C.-C. Yang, C.-T. Yeh, Y.-R. Chen, C.-Y. Li, B.-T. Ko, C.-H. Lin, CrystEngComm **16**, 9308 (2014)
36. M. Zhou, Y. Hu, Y. Liu, W. Yang, H. Qian, CrystEngComm **14**, 7686 (2012)
37. J.K. Vaishnav, S.S. Arbuj, S.B. Rane, D.P. Amalnerkar, RSC Adv. **4**, 47637 (2014)
38. T. Cetinkaya, U. Tocoglu, M. Uysal, M.O. Guler, H. Akbulut, Microelectron. Eng. **126**, 54 (2014)
39. Z. Cui, Y. Zhang, S. Li, S. Ge, Catal. Commun. **72**, 97 (2015)
40. O. Mendiuk, M. Nawrocki, L. Kepinski, Ceram. Int. **42**, 1998 (2016)
41. R. Adhikari, G. Gyawali, T.H. Kim, T. Sekino, S.W. Lee, Mater. Lett. **91**, 294 (2013)
42. M.L. Moreira, G.P. Mambrini, D.P. Volanti, E.R. Leite, M.O. Orlandi, P.S. Pizani, V.R. Mastelaro, C.O. Paiva-Santos, E. Longo, J.A. Varela, Chem. Mater. **20**, 5381 (2008)
43. A. Rizzuti, M. Dassisti, P. Mastrorilli, M.C. Sportelli, N. Cioffi, R.A. Picca, E. Agostinelli, G. Varvaro, R. Caliandro, J. Nanopart. Res. **17**, 408 (2015)
44. K. Byrappa, T. Ohachi, *Crystal Growth Technology* (William Andrew Pub. ;Springer, Norwich, N.Y. Berlin; New York, 2003)
45. K. Byrappa, M. Yoshimura, *Handbook of Hydrothermal Technology: A Technology for Crystal Growth and Materials Processing, 1st ed* (Noyes Publications, Park Ridge, 2001)
46. M. Yoshimura, K. Byrappa, J. Mater. Sci. **43**, 2085 (2008)
47. K. Byrappa, T. Adschiri, Prog. Cryst. Growth Charact. Mater. **53**, 117 (2007)
48. S. Diodati, P. Dolcet, M. Casarin, S. Gross, Chem. Rev. **115**(20), 11449 (2015)
49. I. Bilecka, M. Niederberger, Nanoscale **2**, 1358 (2010)
50. R.S. Varma, Green Chem. **1**, 43 (1999)
51. V. Polshettiwar, R.S. Varma, Acc. Chem. Res. **41**, 629 (2008)
52. V. Polshettiwar, M.N. Nadagouda, R.S. Varma, Aust. J. Chem. **62**, 16 (2009)
53. M.N. Nadagouda, R.S. Varma, Cryst. Growth Des. **8**, 291 (2008)
54. V. Polshettiwar, R.S. Varma, Green Chem. **12**, 743 (2010)
55. V. Polshettiwar, R.S. Varma, Chem. Soc. Rev. **37**, 1546 (2008)
56. V. Polshettiwar, R.S. Varma, Curr. Opin. Drug Discov. Dev. **10**, 723 (2007)
57. B. Baruwati, V. Polshettiwar, R.S. Varma, Green Chem. **11**, 926 (2009)
58. C. Gabriel, S. Gabriel, E.H. Grant, B.S.J. Halstead, D.M.P. Mingos, Chem. Soc. Rev. **27**, 213 (1998)
59. D.M.P. Mingos, D.R. Baghurst, Chem. Soc. Rev. **20**, 1 (1991)
60. B. L. Hayes, *Microwave Synthesis: Chemistry at the Speed of Light* (CEM Publishing, 2002)
61. M.B. Gawande, S.N. Shelke, R. Zboril, R.S. Varma, Acc. Chem. Res. **47**, 1338 (2014)
62. J.-S. Schanche, Mol. Divers. **7**, 291 (2003)
63. A. de la Hoz, A. Diaz-Ortiz, A. Moreno, Chem. Soc. Rev. **34**, 164 (2005)
64. K. Huang, X. Yang, W. Hua, G. Jia, L. Yang, New J. Chem. **33**, 1486 (2009)
65. C. Antonio, R.T. Deam, Phys. Chem. Chem. Phys. **9**, 2976 (2007)
66. J. Robinson, S. Kingman, D. Irvine, P. Licence, A. Smith, G. Dimitrakis, D. Obermayer, C.O. Kappe, Phys. Chem. Chem. Phys. **12**, 4750 (2010)
67. M.R. Rosana, Y. Tao, A.E. Stiegman, G.B. Dudley, Chem. Sci. **3**, 1240 (2012)
68. J.-Y. Li, S. Xiong, J. Pan, Y. Qian, J. Phys. Chem. C (2010)
69. D.P. Volanti, M.O. Orlandi, J. Andres, E. Longo, CrystEngComm **12**, 1696 (2010)
70. L. Qin, J. Xu, X. Dong, Q. Pan, Z. Cheng, Q. Xiang, F. Li, Nanotechnology **19**, 185705 (2008)
71. A. Birkel, F. Reuter, D. Koll, S. Frank, R. Branscheid, M. Panthofer, E. Rentschler, W. Tremel, CrystEngComm **13**, 2487 (2011)
72. S. Xuan, Y.-X.J. Wang, J.C. Yu, K. Cham-Fai Leung, Chem. Mater. **21**, 5079 (2009)
73. H. Zhang, J. Feng, T. Fei, S. Liu, T. Zhang, Sensors Actuators B Chem. **190**, 472 (2014)
74. G. Neri, S.G. Leonardi, M. Latino, N. Donato, S. Baek, D.E. Conte, P.A. Russo, N. Pinna, Sensors Actuators B Chem. **179**, 61 (2013)
75. Z. Ai, L. Zhang, S. Lee, W. Ho, J. Phys. Chem. C **113**, 20896 (2009)
76. X. Zou, H. Fan, Y. Tian, M. Zhang, X. Yan, Dalton Trans. **44**, 7811 (2015)
77. P. Rai, W.-K. Kwak, Y.-T. Yu, ACS Appl. Mater. Interfaces **5**, 3026 (2013)
78. R. Krishnapriya, S. Praneetha, A. Vadivel Murugan, CrystEngComm **17**, 8353 (2015)
79. J. Chen, H. Bin Yang, J. Miao, H.-Y. Wang, B. Liu, J. Am. Chem. Soc. **136**, 15310 (2014)
80. K. Manseki, Y. Kondo, T. Ban, T. Sugiura, T. Yoshida, Dalton Trans. **42**, 3295 (2013)
81. G. Wulff, Z. Kryst. Mineral **34**, 449 (1901)
82. H. Zhang, M. Jin, Y. Xiong, B. Lim, Y. Xia, Acc. Chem. Res. **46**, 1783 (2013)
83. J. Andrés, L. Gracia, A.F. Gouveia, M.M. Ferrer, E. Longo, Nanotechnology **26**, 405703 (2015)
84. H. Cölfen, *Mesocrystals and Nonclassical Crystallization, 1st ed* (John Wiley & Sons Ltd, Chichester, 2008)
85. J.W. Mullin, *Crystallization, 4th ed* (Butterworth-Heinemann, Oxford, 2001)
86. H. Cölfen, S. Mann, Angew. Chemie Int. Ed. **42**, 2350 (2003)
87. W. Ostwald, Z. Phys. Chem. Stochiometrie Verwandtschaftslehre **34** (1900)
88. Z. Wu, S. Yang, W. Wu, Nanoscale **8**, 1237 (2016)
89. W. Chen, H. Ruan, Y. Hu, D. Li, Z. Chen, J. Xian, J. Chen, X. Fu, Y. Shao, Y. Zheng, CrystEngComm **14**, 6295 (2012)
90. Z. Kozakova, I. Kuritka, N.E. Kazantseva, V. Babayan, M. Pastorek, M. Machovsky, P. Bazant, P. Saha, Dalton Trans. **44**, 21099 (2015)
91. A.P. Moura, L.S. Cavalcante, J.C. Sczancoski, D.G. Stroppa, E.C. Paris, A.J. Ramirez, J.A. Varela, E. Longo, Adv. Powder Technol. **21**, 197 (2010)

92. G.J. Wilson, A.S. Matijasevich, D.R.G. Mitchell, J.C. Schulz, G.D. Will, Langmuir **22**, 2016 (2006)
93. R.L. Penn, J.F. Banfield, Science (80-.) **281**, 969 (1998)
94. M. Niederberger, H. Cölfen, Phys. Chem. Chem. Phys. **8**, 3271 (2006)
95. N.T.K. Thanh, N. Maclean, S. Mahiddine, Chem. Rev. **114**, 7610 (2014)
96. R.L. Penn, J.A. Soltis, CrystEngComm **16**, 1409 (2014)
97. M. Distaso, M. Mačković, E. Spiecker, W. Peukert, Chemistry **20**, 8199 (2014)
98. S.-W. Cao, Y.-J. Zhu, Nanoscale Res. Lett. **6**, 1 (2010)
99. C.-Y. Cao, Z.-M. Cui, C.-Q. Chen, W.-G. Song, W. Cai, J. Phys. Chem. C **114**, 9865 (2010)
100. S. Vijayakumar, S. Nagamuthu, G. Muralidharan, ACS Appl. Mater. Interfaces **5**, 2188 (2013)
101. T.M. Perfecto, C.A. de Zito, D.P. Volanti, RSC Adv. **6**, 105171 (2016)
102. S. Komarneni, R. Roy, Q.H. Li, Mater. Res. Bull. **27**, 1393 (1992)
103. M. Baghbanzadeh, L. Carbone, P.D. Cozzoli, C.O. Kappe, Angew. Chem. Int. Ed. **50**, 11312 (2011)
104. C.O. Kappe, D. Dallinger, Nat. Rev. Drug Discov. **5**, 51 (2006)
105. C.O. Kappe, Chem. Soc. Rev. **37**, 1127 (2008)
106. D. Dallinger, C.O. Kappe, Chem. Rev. **107**, 2563 (2007)
107. S. Komarneni, D.S. Li, B. Newalkar, H. Katsuki, A.S. Bhalla, Langmuir **18**, 5959 (2002)
108. O.V. Belousov, N.V. Belousova, A.V. Sirotina, L.A. Solovyov, A.M. Zhyzhaev, S.M. Zharkov, Y.L. Mikhlin, Langmuir **27**, 11697 (2011)
109. H.L. Nguyen, L.E.M. Howard, S.R. Giblin, B.K. Tanner, I. Terry, A.K. Hughes, I.M. Ross, A. Serres, H. Bürckstümmer, J.S.O. Evans, J. Mater. Chem. **15**, 5136 (2005)
110. P.N. Njoki, L.V. Solomon, W. Wu, R. Alam, M.M. Maye, Chem. Commun. (Camb.) **47**, 10079 (2011)
111. W. Wu, P.N. Njoki, H. Han, H. Zhao, E.A. Schiff, P.S. Lutz, L. Solomon, S. Matthews, M.M. Maye, J. Phys. Chem. C **115**, 9933 (2011)
112. Y. Wang, J. Tian, C. Fei, L. Lv, X. Liu, Z. Zhao, G. Cao, J. Phys. Chem. C **118**, 25931 (2014)
113. Z. Wang, X. Zhou, Z. Li, Y. Zhuo, Y. Gao, Q. Yang, X. Li, G. Lu, RSC Adv. **4**, 23281 (2014)
114. A. Pimentel, D. Nunes, P. Duarte, J. Rodrigues, F.M. Costa, T. Monteiro, R. Martins, E. Fortunato, J. Phys. Chem. C **118**, 14629 (2014)
115. X. Li, S. Yao, J. Liu, P. Sun, Y. Sun, Y. Gao, G. Lu, Sensors Actuators B Chem. **220**, 68 (2015)
116. K. Manseki, T. Sugiura, T. Yoshida, New J. Chem. **38**, 598 (2014)
117. A. Phuruangrat, D.J. Ham, S.J. Hong, S. Thongtem, J.S. Lee, J. Mater. Chem. **20**, 1683 (2010)
118. J. Sungpanich, T. Thongtem, S. Thongtem, Ceram. Int. **38**, 1051 (2012)
119. T.M. Perfecto, C.A. Zito, D.P. Volanti, CrystEngComm **19**, 2733 (2017)
120. P. Rai, H.-M. Song, Y.-S. Kim, M.-K. Song, P.-R. Oh, J.-M. Yoon, Y.-T. Yu, Mater. Lett. **68**, 90 (2012)
121. R.A. Silva, M.O. Orlandi, J. Nanomater., 4054058 (2016)
122. F.V. Motta, R.C. Lima, A.P.A. Marques, E.R. Leite, J.A. Varela, E. Longo, Mater. Res. Bull. **45**, 1703 (2010)
123. K. Chen, Y. Dong Noh, W. Huang, J. Ma, S. Komarneni, D. Xue, Ceram. Int. **40**, 2877 (2014)
124. M. Song, P. Rai, K.-J. Ko, S.-H. Jeon, B.-S. Chon, C.-H. Lee, Y.-T. Yu, RSC Adv. **4**, 3529 (2014)
125. P.-S. Shen, Y.-C. Tai, P. Chen, Y.-C. Wu, J. Power Sources **247**, 444 (2014)
126. S. Yoon, E.-S. Lee, A. Manthiram, Inorg. Chem. **51**, 3505 (2012)
127. Y. Yang, G. Wang, Q. Deng, D.H.L. Ng, H. Zhao, ACS Appl. Mater. Interfaces **6**, 3008 (2014)
128. K.F. Moura, J. Maul, A.R. Albuquerque, G.P. Casali, E. Longo, D. Keyson, A.G. Souza, J.R. Sambrano, I.M.G. Santos, J. Solid State Chem. **210**, 171 (2014)
129. A.A. Al-Ghamdi, F. Al-Hazmi, O.A. Al-Hartomy, F. El-Tantawy, F. Yakuphanoglu, J. Sol-Gel Sci. Technol. **63**, 187 (2012)
130. V. Polshettiwar, B. Baruwati, R.S. Varma, ACS Nano **3**, 728 (2009)
131. Z. Moorhead-Rosenberg, K.L. Harrison, T. Turner, A. Manthiram, Inorg. Chem. **52**, 13087 (2013)
132. S. Ghosh, P. Kar, N. Bhandary, S. Basu, S. Sardar, T. Maiyalagan, D. Majumdar, S. K. Bhattacharya, A. Bhaumik, P. Lemmens, S. K. Pal, Catal. Sci. Technol. (2016)
133. J. Sodtipinta, H.-K. Kim, S.-W. Lee, S.M. Smith, P. Pakawatpanurut, K.-B. Kim, J. Electroceram. **35**, 111 (2015)
134. G. Anandha Babu, G. Ravi, T. Mahalingam, M. Kumaresavanji, Y. Hayakawa, Dalton Trans. **44**, 4485 (2015)
135. T.A. Mulinari, F.A. La Porta, J. Andrés, M. Cilense, J.A. Varela, E. Longo, CrystEngComm **15**, 7443 (2013)
136. S. Schmidt, E.T. Kubaski, D.P. Volanti, T. Sequinel, V.D.N. Bezzon, A. Beltrán, S.M. Tebcherani, J.A. Varela, Inorg. Chem. (2015)
137. G. Qiu, S. Dharmarathna, Y. Zhang, N. Opembe, H. Huang, S.L. Suib, J. Phys. Chem. C **116**, 468 (2012)
138. D.P. Volanti, A.G. Sato, M.O. Orlandi, J.M.C. Bueno, E. Longo, J. Andres, ChemCatChem **3**, 839 (2011)
139. C. Sun, X. Su, F. Xiao, C. Niu, J. Wang, Sensors Actuators B Chem. **157**, 681 (2011)
140. S. Chen, Y. Zhao, B. Sun, Z. Ao, X. Xie, Y. Wei, G. Wang, ACS Appl. Mater. Interfaces **7**, 3306 (2015)
141. X. Liu, L. Pan, T. Lv, Z. Sun, C.Q. Sun, J. Colloid Interface Sci. **408**, 145 (2013)
142. A.E. Souza, S.R. Teixeira, C.M. -Santos, W.H. Schreiner, P.N. Lisboa Filho, E. Longo, J. Mater. Chem. C **2**, 7056 (2014)
143. I. Velasco-Davalos, F. Ambriz-Vargas, G. Kolhatkar, R. Thomas, A. Ruediger, AIP Adv. **6**, 65117 (2016)
144. G. Kolhatkar, F. Ambriz-Vargas, R. Thomas, A. Ruediger, Cryst. Growth Des. **17**, 5697 (2017)
145. V. Swaminathan, S.S. Pramana, T.J. White, L. Chen, R. Chukka, R.V. Ramanujan, ACS Appl. Mater. Interfaces **2**, 3037 (2010)
146. L.M. Lozano-Sánchez, S.-W. Lee, T. Sekino, V. Rodríguez-González, CrystEngComm **15**, 2359 (2013)
147. T.M. Mazzo, G.S. Do Nascimento Libanori, M.L. Moreira, W. Avansi, V.R. Mastelaro, J.A. Varela, E. Longo, J. Lumin. **165**, 130 (2015)
148. M.L. Moreira, J. Andrés, V.R. Mastelaro, J.A. Varela, E. Longo, CrystEngComm **13**, 5818 (2011)
149. K. De Keukeleere, J. Feys, M. Meire, J. De Roo, K. De Buysser, P. Lommens, I. Van Driessche, J. Nanopart. Res. **15**, 2074 (2013)
150. I. Janowska, K. Chizari, O. Ersen, S. Zafeiratos, D. Soubane, V. da Costa, V. Speisser, C. Boeglin, M. Houllé, D. Begin, D. Plee, M.J. Ledoux, C. Pham-Huu, Nano Res. **3**, 126 (2010)
151. S. Vadahanambi, J.H. Jung, I.K. Oh, Carbon N. Y. **49**, 4449 (2011)
152. H. Hu, Z. Zhao, Q. Zhou, Y. Gogotsi, J. Qiu, Carbon N. Y. **50**, 3267 (2012)
153. J. Long, M. Fang, G. Chen, J. Mater. Chem. **21**, 10421 (2011)
154. M. M. Viana, M. C. F. S. Lima, J. C. Forsythe, M. Cho, Y. Cheng, G. G. Silva, and M. S. Wong, **26**, 978 (2015)
155. S.J.A. Moniz, J. Tang, ChemCatChem **7**, 1595 (2015)
156. J. Geng, G.-H. Song, X.-D. Jia, F.-F. Cheng, J.-J. Zhu, J. Phys. Chem. C **116**, 4517 (2012)
157. W. Yang, P. Wan, X. Zhou, J. Hu, Y. Guan, L. Feng, ACS Appl. Mater. Interfaces **6**, 21093 (2014)
158. J. Huang, G. Tan, H. Ren, W. Yang, C. Xu, C. Zhao, A. Xia, ACS Appl. Mater. Interfaces **6**, 21041 (2014)
159. P. Rai, S.M. Majhi, Y.-T. Yu, J.-H. Lee, RSC Adv. **5**, 17653 (2015)

160. N. Garino, A. Sacco, M. Castellino, J.A. Muñoz, A. Chiodoni, V. Agostino, V. Margaria, M. Gerosa, G. Massaglia, M. Quaglio, ACS Appl. Mater. Interfaces (2016)
161. D. Wang, X. Li, J. Wang, J. Yang, D. Geng, R. Li, M. Cai, T.-K. Sham, X. Sun, J. Phys. Chem. C **116**, 22149 (2012)
162. C. Zhong, J. Wang, Z. Chen, H. Liu, J. Phys. Chem. C **115**, 25115 (2011)
163. L. Li, K.H. Seng, H. Liu, I.P. Nevirkovets, Z. Guo, Electrochim. Acta **87**, 801 (2013)
164. C.-L. Liu, K.-H. Chang, C.-C. Hu, W.-C. Wen, J. Power Sources **217**, 184 (2012)
165. Q. Xiang, J. Yu, M. Jaroniec, Nano **3**, 3670 (2011)
166. L.Q. Lu, Y. Wang, J. Mater. Chem. **21**, 17916 (2011)
167. W. Zhou, F. Zhang, S. Liu, J. Wang, X. Du, D. Yin, L. Wang, RSC Adv. **4**, 51362 (2014)
168. Z. Wang, Y. Xiao, X. Cui, P. Cheng, B. Wang, Y. Gao, X. Li, T. Yang, T. Zhang, G. Lu, ACS Appl. Mater. Interfaces **6**, 3888 (2014)
169. S.-H. Park, H.-K. Kim, K.C. Roh, K.-B. Kim, Electron. Mater. Lett. **11**, 282 (2015)
170. Y. Zou, J. Kan, Y. Wang, J. Phys. Chem. C **115**, 20747 (2011)
171. L. Kashinath, K. Namratha, K. Byrappa, Appl. Surf. Sci. **357**, 1849 (2015)
172. R. Sharma, F. Alam, A.K. Sharma, V. Dutta, S.K. Dhawan, J. Mater. Chem. C **2**, 8142 (2014)
173. Y. Gui, Z. Liu, S. Fang, J. Tian, F. Gong, J. Mater. Sci. Mater. Electron. (2015)
174. Y. Gui, J. Zhao, W. Wang, J. Tian, M. Zhao, Mater. Lett. **155**, 4 (2015)
175. C.A. Zito, T.M. Perfecto, D.P. Volanti, Sensors Actuators B Chem. **244**, 466 (2017)
176. M. Chen, Z. Wang, D. Han, F. Gu, G. Guo, J. Phys. Chem. C **115**, 12763 (2011)
177. Z. Wang, P. Sun, T. Yang, Y. Gao, X. Li, G. Lu, Y. Du, Sensors Actuators B Chem. **186**, 734 (2013)
178. Q. Wang, C. Wang, H. Sun, P. Sun, Y. Wang, J. Lin, G. Lu, Sensors Actuators B Chem. **222**, 257 (2016)
179. Y.-S. Kim, P. Rai, Y.-T. Yu, Sensors Actuators B Chem. **186**, 633 (2013)
180. T. Yanagimoto, Y.-T. Yu, K. Kaneko, Sens. Actuators **B 166–167**, 31 (2012)
181. L.M. Sikhwivhilu, S. Mpelane, B.W. Mwakikunga, S. Sinha Ray, ACS Appl. Mater. Interfaces **4**, 1656 (2012)
182. R.D. Martínez-Orozco, R. Antaño-López, V. Rodríguez-González, New J. Chem. **39**, 8044 (2015)
183. P. Sun, C. Wang, J. Liu, X. Zhou, X. Li, X. Hu, G. Lu, ACS Appl. Mater. Interfaces **7**, 19119 (2015)
184. C. Yang, X. Su, J. Wang, X. Cao, S. Wang, L. Zhang, Sensors Actuators B Chem. **185**, 159 (2013)
185. C. Yang, X. Su, F. Xiao, J. Jian, J. Wang, Sensors Actuators B Chem. **158**, 299 (2011)
186. C.A. Zito, T.M. Perfecto, D.P. Volanti, Adv. Mater. Interfaces **4**, 1700847 (2017)
187. D.P. Volanti, A.A. Felix, M.O. Orlandi, G. Whitfield, D.-J. Yang, E. Longo, H.L. Tuller, J.A. Varela, Adv. Funct. Mater. **23**, 1759 (2013)
188. S. Kong, R. Dai, H. Li, W. Sun, Y. Wang, ACS Sustain. Chem. Eng. **3**, 1830 (2015)
189. W.X. Chen, J.Y. Lee, Z.L. Liu, Chem. Commun. **2588** (2002)
190. S. Ghosh, P. Kar, N. Bhandary, S. Basu, S. Sardar, T. Maiyalagan, D. Majumdar, S. K. Bhattacharya, A. Bhaumik, P. Lemmens, S. K. Pal, Cat. Sci. Technol. (2016)
191. G. Byzynski, A.P. Pereira, D.P. Volanti, C. Ribeiro, E. Longo, J. Photochem. Photobiol. A Chem. **353**, 358 (2018)
192. M. Yang, B. Ding, S. Lee, J.-K. Lee, J. Phys. Chem. C **115**, 14534 (2011)
193. L. Liu, K. Hong, X. Ge, D. Liu, M. Xu, J. Phys. Chem. C **118**, 15551 (2014)
194. A. Birkel, Y.-G. Lee, D. Koll, X. Van Meerbeek, S. Frank, M.J. Choi, Y.S. Kang, K. Char, W. Tremel, Energy Environ. Sci. **5**, 5392 (2012)